Geological factors and fracture distribution in deep and ultra-deep sandstones in Kuqa Depression, Tarim Basin, China

Yang Su[1,2], Jin Lai[1,2], Wenle Dang[2], Xinjian Zhao[3], Chuang Han[3], Yongjia Zhang[2], Zhongrui Wang[2], Lei Wang[2], Guiwen Wang[1,2]

[1]National Key Laboratory of Petroleum Resources and Engineering, China University of Petroleum (Beijing), Beijing, 102249, China
[2]College of Geosciences, China University of Petroleum (Beijing), Beijing, 102249, China
[3]Research Institute of Petroleum Exploration and Development, Tarim Oilfield Company, CNPC, Korla, 841000, Xinjiang, China

Correspondence to: Yang Su (suyangcupb@163.com)

Abstract. Deep (>4500 m) and ultra-deep (>6000 m) sandstone reservoirs hold great potential for hydrocarbon resources, yet complex geological challenges hinder the successful exploitation of oil and gas. Fractures in deep and ultra-deep sandstones are prevalent and significantly enhance rock permeability, and critically impact fluid flow and hydrocarbon productivity. Relationships between geological factors and fracture distribution in deep sandstone reservoirs, despite its significance, have remained poorly understood. This study utilizes core, thin section, acoustic emission tests and geophysical well logs to elucidate the interplay between geological elements and fracture occurrences in tight sandstones of the Kuqa Depression, which is a tectonically active foreland basin. The controls of sedimentation, sandbody distribution and earth stress on fracture distribution are analyzed. The research then unravels the effects of lithology units, earth stress fields, and broader tectonic context on fracture distribution patterns. Geological factors, including sedimentary factors (lithology, sandbody thickness and sandbody distribution), earth stress, and tectonic structure are integrated to comprehensively evaluate the fracture distributions in Kuqa Depression. The different lithologies are identified, and fractures in different lithologies are characterized. High-angle fractures and vertical fractures are the main fracture types in Bozi-Dabei area. Fracture density exhibits an inverse relationship with sandbody thickness. The presence of thinner sandstones in conjunction with thin mud layers facilitates the formation of fractures. Paleostress affects the generation of natural fractures, and high fracture density is associated with high paleostress magnitudes. In situ stress affects the subsequent modification of natural fractures. However, some filled fractures with wider aperture oriented at high angles to S_{Hmax} reveal cement-stress interactions jointly controlling apertures, not stress dominance. Structure factors including the position at folds and the proximity to faults are crucial for the fracture distribution. Fractures are more abundant in the hinge areas of anticlines compared to the limb areas, and fracture density above the neutral planes is notably higher. In addition, fracture density is higher in the formation adjacent to the fault due to the effect of the regional stress field. This study helps unravel the geological controlling factors and distribution of fractures by integrating geological and geophysical data, and has implications for hydrocarbon resource exploration in deep and ultra-deep sandstones.

1 Introduction

Fractures in ultra-deep (>6000 m) sandstones represent a critical frontier in geoscience with profound implications for hydrocarbon exploration and reservoir evaluation. Fractures are prevalent in deep (typically >4500 m) and ultra-deep (typically >6000 m) reservoirs and fracture-induced heterogeneities can significantly increase permeability and productivity in rocks (e.g., Laubach, 2003; Ghosh and Mitra, 2009; Olson et al., 2009; Laubach et al., 2019; Chen et al., 2021; Cawood et al., 2023; Laubach et al., 2023). Fractures in deep and ultra-deep tight sandstones have a major impact on fluid flow, controlling reservoir connectivity, and determining reservoir properties (Laubach, 2003; Zeng et al., 2013; Laubach et al., 2019; Zeng et al., 2023; Laubach et al., 2023). Fractures play a crucial role in environmental and energy resource issues (e.g., Nelson, 1985; Gale et al., 2014; Laubach et al., 2019; Zeng et al., 2023; Laubach et al., 2023; Romano et al., 2025; Gong et al., 2025). Understanding the complex geological factors affecting fracture distribution in deep and ultra-deep sandstone reservoirs is essential for optimizing hydrocarbon recovery, improving reservoir delineation, and assessing risks effectively (Hank et al., 1997; Zeng, 2010; Launch et al., 2019; Feng et al., 2023; Zeng et al., 2023). Geophysical well logs including conventional well logs, image logs, and array acoustic logs provide crucial insights into the rock's physical properties, compositional variations, and structural discontinuities at depth (e.g., Pang et al., 2023; Lai et al., 2023; Lai et al., 2024; Zhang et al., 2024; Medici et al., 2024). A comprehensive approach integrating geological data and geophysical well logs can reveal relationships between geological factors and fracture distribution.

A growing body of research indicates that natural fractures are controlled by many factors including structural factors and sedimentary factors (e.g., Nelson, 1985; Jamison, 1997; Feng et al., 2019; Douma et al., 2019; Sun et al., 2021; Zeng et al., 2023; Cawood et al., 2023; Laubach et al., 2023). The complex interplay between structural controls (structural position, faults and in-situ stress) and sedimentary factors (lithology and sandbody distribution) complicates fracture occurrence and distribution prediction (e.g., Friedman, 1969; Ghosh and Mitra, 2009; Frehner, 2011; Douma et al., 2019; Feng et al., 2019; Ogata et al., 2019; Zhao et al.,2021; Yang et al., 2022; Laubach et al., 2023). There are multiple factors influencing on distribution of fractures in sandstones, and they include the inherent mechanical characteristics of lithological units, regional stress fields, and structure (e.g., Hank et al., 1997; Ghosh and Mitra, 2009; Frehner, 2011; Feng et al., 2019; Lai et al., 2019; Cawood et al., 2023; Laubach et al., 2023). Lithology, particularly the different carbonate facies, significantly influences fracture distribution by affecting the mechanical properties and susceptibility to deformation (e.g., Hank et al., 1997; Mercuri et al., 2020; Cawood et al., 2023; Gong et al., 2025). Laubach et al. (2019) reveal that Fractures in rocks control fluid flow and rock strength. Chemical reactions (mineral growth/dissolution) play a bigger role in fracture development than previously thought (e.g., Laubach et al., 2004; Lander and Laubach, 2015; Laubach et al., 2019). The distribution, orientation, and behavior of natural and induced fractures in subsurface formations are fundamentally governed by the in-situ stress field (eg. Zoback, 2007; Lai et al., 2019; Guo et al., 2019; Zhang and Ma, 2021; Yu et al., 2023; Zeng et al., 2023). The differential stress ratio (S_{Hmax}/S_{hmin}) and pore pressure control fracture shear reactivation and dilation (eg. Barton et al., 1995; Zeng et al., 2023). Structure is the crucial factor controlling the fracture distribution (e.g., Friedman, 1969; Hanks et al., 1997; Jamison,

1997; Ghosh and Mitra, 2009; Cawood et al., 2023; Zeng et al., 2023). Apart from the thickness of sandstones and the lithology of the rocks, fracture density is also influenced by structural location, such as the proximity to fault, and is related to its location within the folds (e.g., Friedman et al., 1969; Jamison et al., 1997; Ghosh and Mitra, 2009; Ju et al., 2014; Sun et al., 2021; Cawood et al., 2023).

The Kuqa Depression is a foreland basin between the Tianshan Orogenic Belt and the Northern Tarim Uplift to the south in the Tarim Basin. It hosts extensively fractured ultra-deep (>6000 m) Cretaceous Bashijiqike Formation sandstones due to multi-phase tectonism. However, few studies have been performed on clarifying geological factors and fracture distribution in Kuqa Depression using geological and geophysical well logs (Chen et al., 2021; Li et al., 2024). Here we show the relationships between geological factors and fracture distribution in deep and ultra-deep reservoirs in Kuqa Depression. Our analysis establishes that high-angle fractures represent the dominant fracture type in ultra-deep (>6000 m) tight sandstones of the Bozi-Dabei block, with the highest fracture density observed in fine-grained sandstones. An inverse relationship is delineated between sandbody thickness and fracture density, with fracture networks preferentially developed in thin sandstones interbedded with mudstone layers. A positive correlation is quantitatively established between maximum paleostress magnitude and fracture density. Earth stress may influence fracture characteristics, where an increase in the horizontal stress difference leads to a decrease in fracture parameter magnitude. While in situ stress modulates apertures, cementation may counteract closure for some fractures oriented at a high angle to S_{Hmax} where mineral bridges develop due to rapid diagenesis in Kuqa Depression (eg., Laubach et al., 2004; Olson et al., 2007; Laubach et al., 2019). Fracture density is maximized in anticlinal hinges compared to limbs, elevated in upper formations along longitudinal axes, and significantly amplified near faults due to stress field perturbations. Critically, we demonstrate that fracture density directly and quantitatively enhances hydrocarbon productivity, with higher fracture densities correlating with elevated oil production rates. The results show that the fundamental geological controls on fracture distributions in ultra-deep foreland basin reservoirs and provide a predictive framework for targeting high-productivity zones.

2 Geological settings

The Kuqa Depression is a segment of foreland basin that has undergone an intricate evolutionary history spanning Mesozoic and Cenozoic eras (Qiu et al., 2012; Yang et al., 2023). The structural configuration of Kuqa Depression is a testament to the dynamic interplay between northward drift of Indian subcontinent and southward compressive forces exerted by South Tianshan orogenic belt (Lu et al., 1994; Ju et al., 2014; Li et al., 2016; Nian et al., 2017) (Fig. 1). The structural architecture of the Kuqa Depression is characterized by southwest-vergent thrust fault systems, with secondary strike-slip fault components, which developed during the peak compressional phase of the Late Himalayan orogeny (Fig. 1) (Lu et al., 1994; Ju et al., 2014; Lai et al., 2019). The Kuqa Depression contains three sags and four structural belts, including Baicheng, Wushi and Yangxia Sag, Northern monoclines, Kelasu, Qiulitage and Southern Gentle Monoclinal structural belts (Fig. 1A) (Zeng, 2010; Qiu et

al., 2012). The Kelasu belt is partitioned into five blocks including Awat block, Bozi block, Dabei block, Keshen block, and Kela block (Fig. 1B). The structural trace of Bozi-Dabei block is an "S" shape (Fig. 1) (Guo et al., 2016; Yang et al., 2023). Kuqa Depression has experienced three major stages, including a paleo-foreland stage, an extensional stage and a rejuvenated foreland stage (Zeng, 2010; Wu et al., 2019). The compressive tectonic movement within Bozi-Dabei zone began in Late Yanshan epoch and reached its peak intensity in Late Himalayan epoch (Li et al., 2016; Guo et al., 2016; Yang et al., 2023). The most intense tectonic movement occurred during the middle to late depositional phases of Kuqa Depression, significantly contributing to the formation of current structural configuration observed in Bozi-Dabei areas (Fig. 1B) (Yu et al., 2014; Yang et al., 2023).

Triassic lacustrine mudstones and Jurassic coal-bearing strata as source rocks provide a bountiful hydrocarbon endowment. Paleogene Kmugeliemu and Neogene Jidike Formations as cap rocks help preserve oil and gas (Li et al., 2012; Zhao et al., 2023). The inception of regional uplift and erosion during Late Cretaceous has led to the stratigraphic absence of Upper Cretaceous deposits (Jin et al., 2008). Lower Cretaceous strata of the region are characterized by Kapushaliang Group and Bashijiqike Formation. Kapushaliang Group includes Yageliemu Formation (K_1y), Shushanhe Formation (K_1s), and Baxigai Formation (K_1b). Notably, Bashijiqike Formation, which serves as the principal hydrocarbon-bearing stratum, exhibits a conformable contact with subjacent Baxigai Formation. Serving as the primary gas-bearing formation in the Bozi-Dabei Block, the Lower Cretaceous Bashijiqike Formation (K_1bs) occurs at depths of 5000-8000 m. Vertically, it comprises three segments: K_1bs_1, K_1bs_2, and K_1bs_3. There is unconformable contact between Paleocene-Eocene Kumugeliemu Formation and underlying Cretaceous strata, indicating a significant absence in sedimentation (Zeng, 2010; Yu et al., 2016). Characterized by substantial thickness and high hydrocarbon generation intensity, the Triassic-Jurassic lacustrine coal measures represent the primary source rocks. Overlain by an extensively developed, thick gypsum-salt sequence, Bashijiqike Formation is capped regionally (Shen et al., 2017; Lai et al., 2019; Wang et al., 2023; Xu et al., 2025).

Due to the erosion of southern Tianshan Mountain, terrigenous clast was provided for Cretaceous reservoir deposition. The depositional environment of Bashijiqike Formation transitions from south to north and changes from a fan delta to a braided river delta (Nian et al., 2018; Zhang et al., 2021; Li et al., 2024). Comprising braided river delta front deposits, the K_1bs_2 unit contrasts with the fan delta front deposits of the K_1bs_3. Laterally, these sand bodies exhibit considerable thickness, extensive lateral continuity, and broad distribution (Lai et al., 2019; Xu et al.,2025). The lithologies of Bashijiqike Formation are mainly medium-grained sandstones, fine-grained sandstones, mudstones and in some cases conglomerates (Jia and Li, 2008; Lai et al., 2018). Cretaceous Bashijiqike reservoir, which is buried in deep (>4500 m) and ultra-deep (>6000 m) depths, exhibits low porosity and permeability. Owing to high overburden stress and intricate interplay of diagenetic processes, the sandstones are heavily fractured. The fractures provide hydrocarbon storage spaces and substantial enhancement of reservoir permeability (Nian et al., 2017; Sun et al., 2017; Zeng et al., 2023). Comparison reveals that while matrix sandstone permeability is primarily 0.001-0.1 mD, that of fractured sandstone ranges from 1 to 10 mD, differing by 1-3 orders of magnitude (Du et al., 2025).

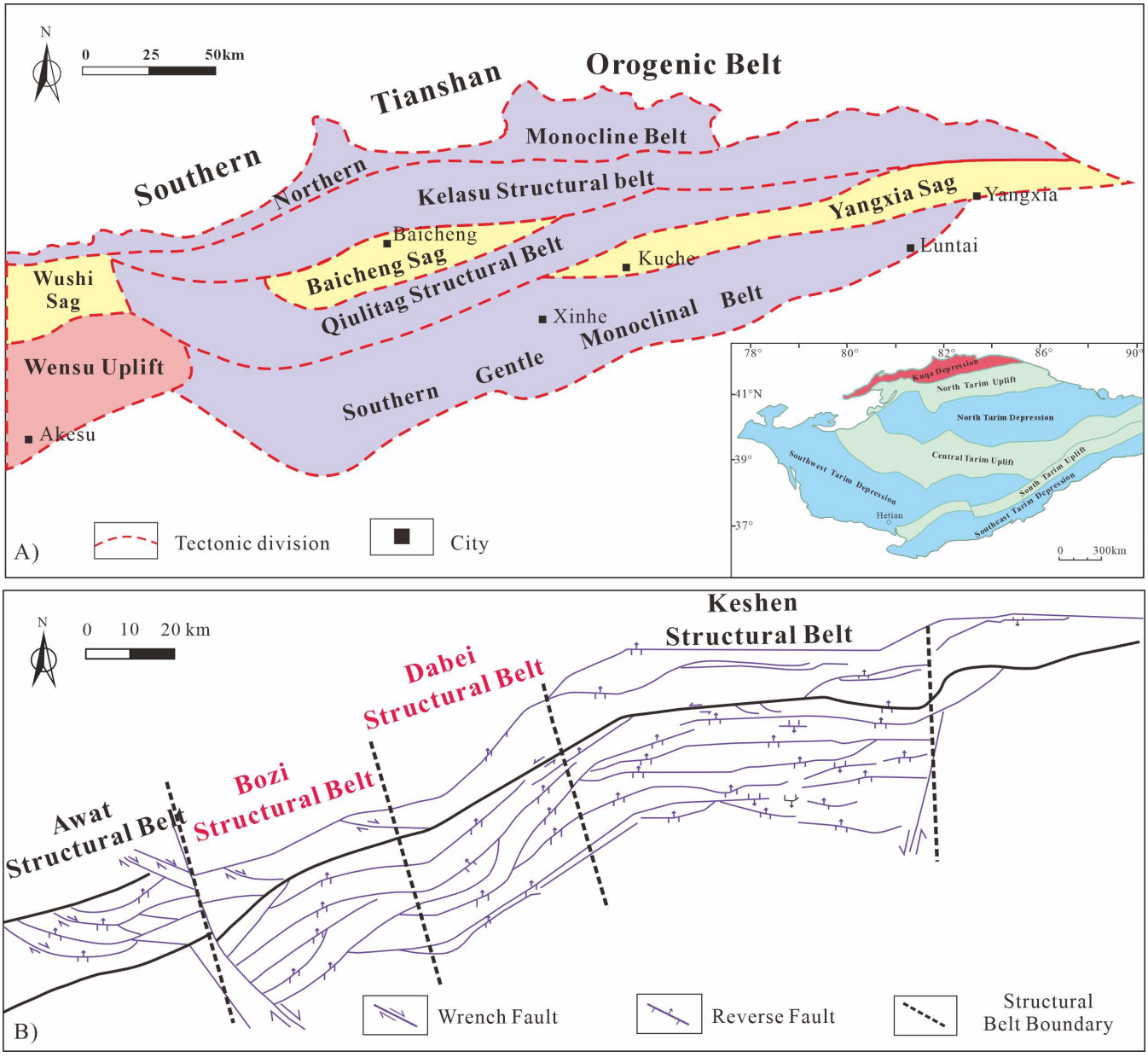

130 **Figure 1: (A) the structural subdivision map of Kuqa Depression; (B) mapping locations of four zones in the Kelasu Thrust Belt (Lai et al., 2021; Song et al., 2024)**

3 Materials and methods

Core samples, which are directly used to observe fracture occurrence and fracture distribution, are collected from 29 wells. The total length of cores can reach up to 284 meters. All analyzed cores and image logs were obtained from depths of 4,500–7,200 m, with fracture characterization focusing in Cretaceous Bashijiqike Formation where fracture networks are most extensively developed.

Thin sections (30 μm thick) were infused with blue-fluorescent epoxy resin to enhance the visibility of pores and micro-fractures. Additionally, thin sections were treated with a staining solution including Alizarin Red and potassium ferricyanide to identify different minerals. The distribution, orientation, and filling materials of microfractures can be analysed by thin sections.

Acoustic emission Test (AE) at Sichuan University quantifies rock stress and infers historical stress conditions. This phenomenon is characterized by a significant increase in AE activity upon surpassing the stress threshold that induced irreversible deformation, such as the propagation of microfracture (Kaiser, 1953; Lavrov, 2003; Guo et al., 2019; Lai et al., 2019). The magnitude of paleostress can be obtained through AE tests.

Image logs provide high-resolution images of the borehole wall, which are essential for detailed geological analysis. A high-definition image log is utilized to capture images of the formation. The fracture characteristics can be observed and fracture parameters can be calculated by image logs. Formation MicroScanner Image (FMI) was run in most of the wells drilled in water-based muds. The workflow for processing FMI data includes Quality Control (QC), Speed Correction, Pad image creation-Button harmonization, Pad concatenation and orientation (creating a static image) and Histogram equalization-Pad concatenation and orientation (creating a dynamic image). Earth Imaging (EI) and QuantaGeo were run in the oil-based muds (Lai et al., 2024).

Array acoustic logs are a type of acoustic well logging that uses an array of transducers to measure the formation's acoustic properties. P-wave time difference, S-wave time difference, and Stoneley wave time difference can be obtained through array acoustic logs, including Dipole Shear Sonic Imager (DSI) and Cross-Multipole Array Acoustic Log (XMAC). The DSI tool (from Schlumberger) uses a combination of monopole and dipole transmitters along with an array of hydrophones to measure these wave velocities (Zahmatkesh et al., 2017). XMAC (from Baker Atlas) operates by combining a monopole array with a dipole array to capture detailed information on the formation's acoustic properties including compressional, shear, and Stoneley wave velocities, as well as amplitude attenuation. Processing involves waveform semblance correction, shear wave splitting quantification to derive fracture density and orientation from fast-shear azimuth (FSA), with Stoneley reflectivity modeling estimating fracture apertures, validated through integration with image logs and anisotropy tensor decomposition.

The ECLIPS-5700 Series tools operate on a variety of measurement principles, including but not limited to natural gamma ray (GR), photoelectric (Pe) log, caliper (CAL), neutron porosity (CNC), bulk density (DEN), sonic interval transit time (DT), and High Definition Induction Resistivity logs (HDIL) (M2Rx, M2R9, M2R6, M2R3, M2R2, M2R1).

Ultrasonic imaging logging (UXPL) also is run in some wells drilled with oil-based muds. UXPL tool provides a high-resolution, 360° view of the borehole wall (Li et al., 2019). Fractures and borehole breakouts over the full circumference of the borehole can be identified by UXPL tool (Lai et al., 2018).

Among various approaches for in-situ stress calculation, One-dimensional Mechanical Earth Models (1-D MEMs) have emerged as the preferred methodology owing to its performance advantages over conventional techniques (Barton et al., 1988; Zoback et al., 2003; Zoback et al., 2007; Tingay et al., 2009). The model effectively represents geological formations as anisotropic media, and incorporates the coupled influence of both Young's modulus and Poisson's ratio in stress calculation (Barton et al., 1988; Zoback et al., 2003; Zoback et al., 2007; Tingay et al., 2009; Tingay et al., 2010). These features make it especially suitable for complex geological environments, as evidenced by its successful application in the Tarim Basin, where it has consistently demonstrated superior predictive capability compared to traditional stress models (Ju and Wang, 2018; Lai et al., 2019).

One-dimensional Mechanical Earth Models (1-D MEMs) enable the determination of in-situ stress magnitudes (S_{Hmax}, S_{hmin}, S_v). Vertical stress (S_v) is calculated by bulk density integration from surface to target depth (Eq.1), with standard gradients at 23 MPa/km (2.3 g/cm³ average density). In the Kuqa Depression, acoustic emission experiments established a gradient of 25.28 MPa/km (2.528 g/cm³), yielding S_v=173.79 MPa at 6,873.38 m. Pore pressure (P_p) is determined using Eaton's sonic transit time method (Eq.2), where deviations from normal compaction trends ($\Delta t_n/\Delta t$) indicate overpressure. Drilling-induced fractures indicate S_{Hmax} direction while breakouts define S_{hmin} orientation using image logs. Log-derived stress calculations incorporate S_{Hmax} and S_{hmin}, with dip corrections applied in steep structures using a modified Anderson model accounting for stratigraphic geometry (Eq.3-4).

$$S_v = \int_0^H \rho g dz \quad (1)$$

$$P_p = P_0 - (P_0 - P_w)(\Delta t_n/\Delta t)^c \quad (2)$$

$$Sh_{min} = (\frac{\nu}{1-\nu} + A - C)(Sv - \alpha P_p) + \alpha P_p \quad (3)$$

$$SH_{max} = (\frac{\nu}{1-\nu} + B - C)(Sv - \alpha P_p) + \alpha P_p \quad (4)$$

Here, S_v is the vertical stress (MPa); H is the burial depth, m; ρ is the bulk density obtained from density (DEN) logs, kg/m^3 and g is the gravitational acceleration (m/s²). P_p represents the formation pressure, while P_0 denotes the overburden pressure; P_w corresponds to the hydrostatic pore pressure. The measured sonic transit time in shale, obtained from well logs, is given by Δt, and Δt_n refers to the normal-compaction sonic transit time in shale, derived from the normal trend line. The exponent c is an empirical constant. ν is Poisson's ratio, calculated using compressional wave velocity (V_p), shear wave velocity (V_s), and bulk density logs. The tectonic stress coefficients A and B are set as 0.405 and 0.891, respectively. C is the coefficient of stratigraphy dip.

4 Results

4.1 Core-scale fractures

Core observations reveal predominantly opening-mode fractures in the Bashijiqike Formation, which can be categorized by angle into low-angle fractures (Fig. 2A), horizontal fractures (Fig.2B), vertical fractures (Fig. 2C), high-angle fractures (Fig. 2D, 2F, 2H) and network fractures (Fig. 2G). Fracture status in the Bashijiqike Formation is recognized as open (Figs. 2B, 2D), semi-filled (Figs. 2C, 2E, 2H), or filled (Figs. 2A, 2F). Fracture observations from cores confirm that high-angle fractures and vertical fractures are the main fracture types in Bozi-Dabei area of Kuqa Depression. Most fractures have straight and smooth surfaces (Fig. 2). As a result of the intricate interplay of multi-phase tectonic processes, fractures intersect at varying angles, establishing fracture network (Fig. 2G). Occasionally, fractures are visible cutting through the gravel (Fig. 2B). Some fractures are partly filled with calcite cement locally observed (Fig. 2H, 2I).

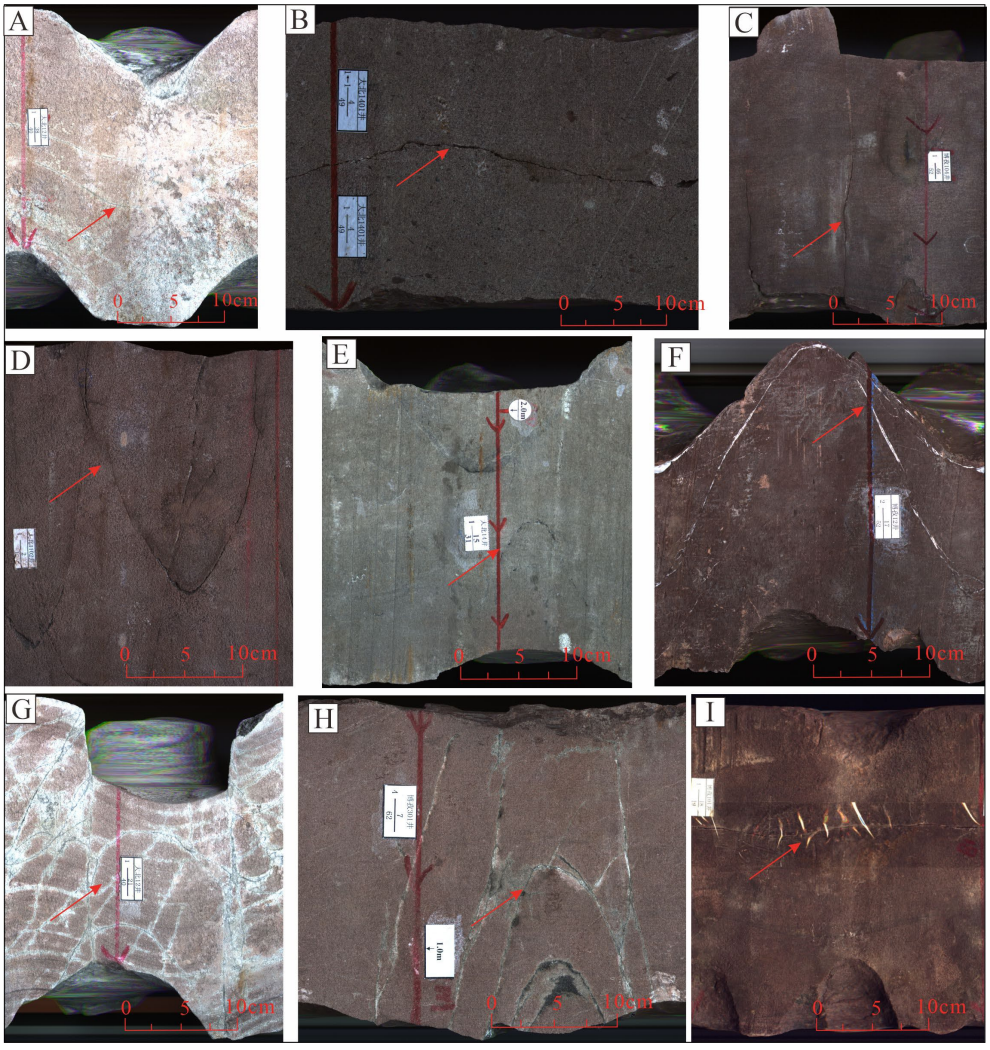

Figure 2: The core photos of various types of core-scale fractures in Bashijiqike Formation in Bozi-Dabei Blocks of Kuqa Depression

A. Closed (calcite-filled) low-angle fracture, Well BZ 12, 5403.85 m

B. Opening-mode horizontal fracture, Well DB 1401, 6351.40 m

C. Vertical fracture, Well BZ 104, 6802.22 m

D. High-angle fracture, Well DB 1102, 5875.11 m

E. Filled fracture (undergo dissolution), Well DB 14, 6349.55 m

F. Filled (calcite filled) fracture, Well BZ 12, 6999.59 m

G. Fracture network, Well DB 12, 5400.04 m

H. Combination of high-angle fracture with different angles, Well BZ 301, 5854.50 m

I. Opening-mode fracture, Well BZ 101, 6918.42 m

4.2 Thin section-scale microfractures

Thin section images can reveal the characteristics of fractures in the micrometer scales. The aperture of micro-fractures varies from 0.01 to 0.04 mm. The aperture of small-scale fractures varies from 0.05 to 0.1 mm. Owing to the resolution limit of well logs, microfractures (< 0.1 mm) can not be observed by well log data. The fractures that were detected in thin sections include micro-fractures and small-scale fractures (Fig. 3). The microfractures can be detected in the fine-medium grained sandstones (Fig. 3A-3C, 3E, 3F), siltstones (Fig. 3D) and in some cases conglomerates (Fig. 3H). Some fractures crosscutting the framework grains (Fig. 3A, 3C, 3I). Fractures show partial to complete cementation by calcite or dolomite (Fig. 3E-3G). Highly connected fracture networks link intergranular and intragranular pores (Fig. 3I).

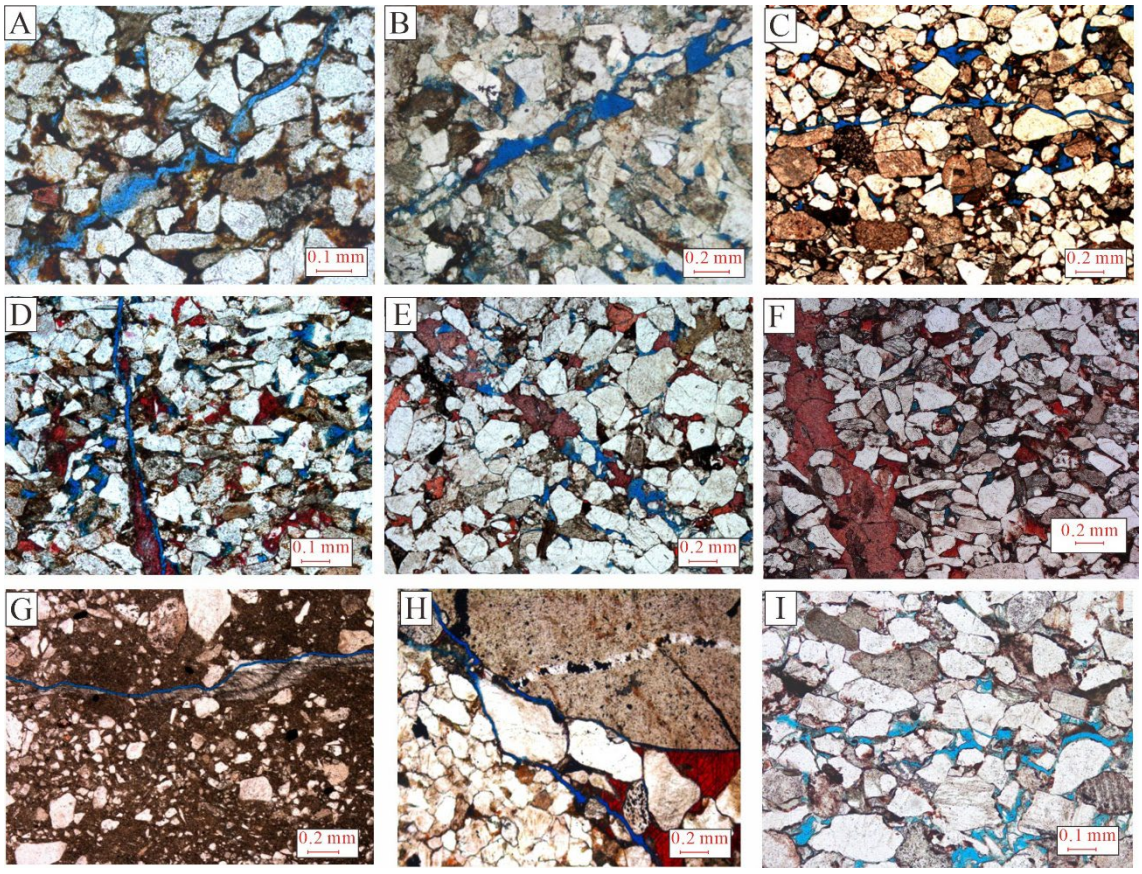

Figure 3: The thin section images of various types of thin section-scale fractures in Bashijiqike Formation in Bozi-Dabei Block of Kuqa Depression

A. **Microfracture crosscutting the framework grains, DB 903, 5178.7 m**

B. **Microfracture in the medium grained sandstones, DB 902, 5099.19 m**

C. **Microfracture crosscutting the framework grains, BZ 9, 7675.95 m**

D. **Microfracture fully cemented by calcite cements coexisting unfilled microfracture, DB 14, 6349.34 m**

E. **Fracture partly cemented by calcite cements, DB 9, 4846.03 m**

F. **Fracture fully cemented by calcite cements, BZ 22, 6328.92 m**

G. **Fracture fully cemented by dolomite cements, BZ 12, 7001.9 m**

H. **Grain boundary microfracture, BZ 302, 6186.85 m**

I. **Microfracture network which link intergranular and intragranular pores, BZ 104, 6802.14 m**

4.3 Log responses of fractures

The presence of fractures in formations drilled with water-based muds is commonly indicated by a reduction of density logs. This reduction is particularly evident when fractures are filled with low-density materials such as drilling muds (Fig.4). Given that the velocity of acoustic waves is slower in liquids compared to solids, the identification of fractures through well logs is accompanied by an increasing interval transit time (AC readings) (Lyu et al., 2016; He et al., 2024) (Fig.4). The value of resistivity around borehole wall can be obtained by image logs. Natural fractures appear as sinusoidal wave appearance in image logs (Fig.4). If fractures are filled with low resistivity materials like water-based muds, fractures represent a dark sinusoidal wave appearance (Khair et al., 2015) (Fig.4). If fractures are filled with high resistivity materials including oil-based muds, gypsum and carbonate cements, the fractures represent bright sinusoidal wave appearances. The fracture parameters including fracture aperture, porosity, density and length can be calculated by Techlog software. The fractures detected in the image logs correspond to those in the cores at the same depth. Meanwhile, the infiltration of muds into fractures leads to an increase in hydrogen content, which in turn, results in an increase in CNL log value (Lai et al., 2017).

The fractures have an absorption and attenuation effect on acoustic waves, which leads to the attenuation of acoustic signals in dipole array sonic logs. The images of full waveforms were provided by array acoustic logging tools. The full waveforms exhibit “V” shape interferometric fringes and the amplitude as well as energy of full-wave waveform show significant attenuation with the presence of conductive fractures (Koerperich et al., 1978) (Fig. 4).

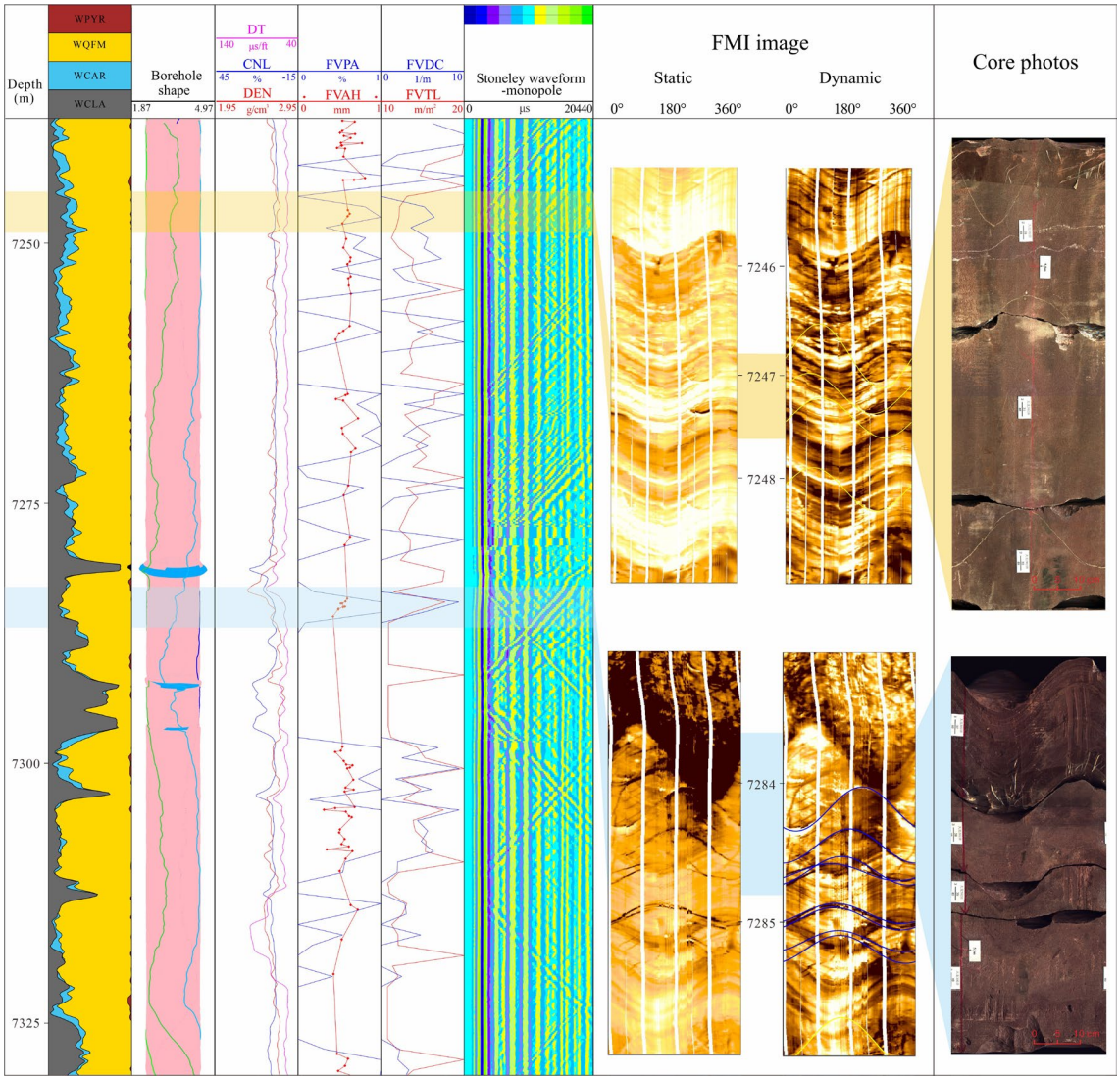

Figure 4: The well log response of fracture in well logs including conventional well logs, image logs, and array acoustic logging in Well DB 302

Track 1: Elemental Capture Spectroscopy (ECS)
Track 3: Compressional wave slowness, Compensated neutron and density logging
Track 4, 5: Fracture parameters including fracture aperture, porosity, density and length
Track 6: Stoneley wave attenuation from array acoustic logging
Track 7: FMI image showing filled fractures (yellow) and conductive fractures (blue)
Track 8: Core photos

4.4 Lithology and fracture distribution

Due to distinct mechanical properties of reservoirs in different lithologies, there are obvious differences in scale and occurrence of fractures generated by the same stress field (Laubach et al., 2009; Lucca et al., 2024). Fine-grained sandstones exhibited higher fracture densities compared with medium-grained sandstones and siltstones (Fig.5). Meanwhile, in medium-grained sandstones, there are also a multitude of fractures can be detected, but not as much as those in fine-grained sandstones.

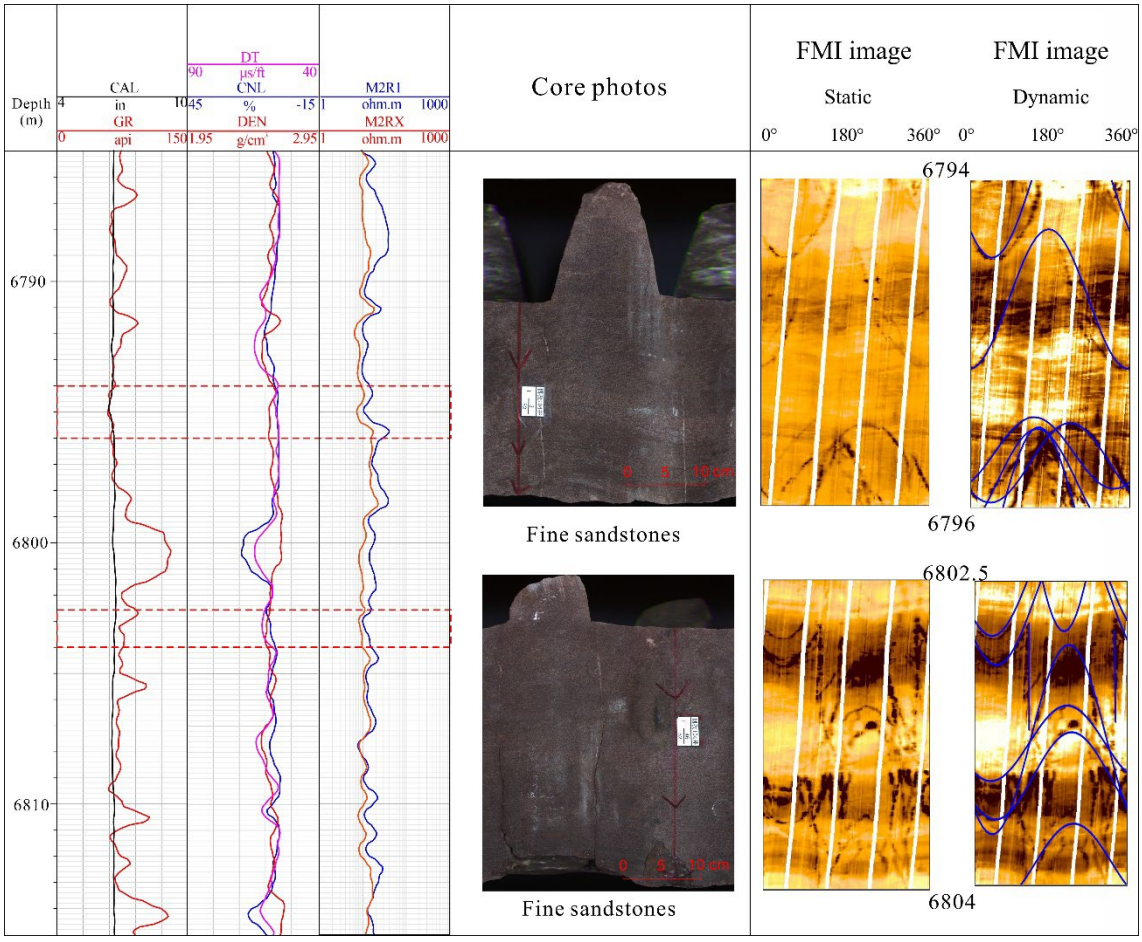

Figure 5: Fracture characteristics in fine-grained sandstones in Well BZ 104 (6, 785-6, 815 m). Core photographs showing fracture density characteristics. Fine-grained sandstone interval (6,802.5-6,804 m) exhibits higher fracture density

4.5 Earth stress calculation

In situ stress affects the late modification of natural fractures (Rajabi et al., 2010; Lai et al., 2019). The maximum principal horizontal stress (S_{Hmax}) magnitude, the minimum principal horizontal stress (S_{hmin}) magnitude, and vertical principal stress (S_v) magnitude can be calculated using Eq. 1-Eq. 4. The vertical stress was calculated using an overburden gradient of 25.28

MPa/km. Maximum (S_{Hmax}) and minimum (S_{hmin}) horizontal stresses were continuously estimated by well logs using Eq. 3-4. While vertical stress (S_v) increases linearly with depth, horizontal stresses exhibit significant fluctuations. Fluid overpressures are prevalent (overpressure coefficient = 1.6-2.2), exemplified at 6440 m depth where horizontal stresses range between 110-200 MPa (Fig.6). The in-situ stress regime corresponds to strike-slip faulting ($S_{Hmax}>S_v>S_{hmin}$) (Fig.6). The differential stress ($\triangle\sigma$) which defined as the difference between the maximum horizontal stress (S_{Hmax}) and the minimum horizontal stress (S_{hmin}) varies between 30 and 50 MPa (Fig.6). The induced fractures are aligned with the direction of S_{Hmax}, and the Breakouts are perpendicular to the direction of S_{Hmax}. Fracture image-log observations reveal that the S_{Hmax} direction trends close to north-south and S_{hmin} direction trends close to west-east (Fig.6).

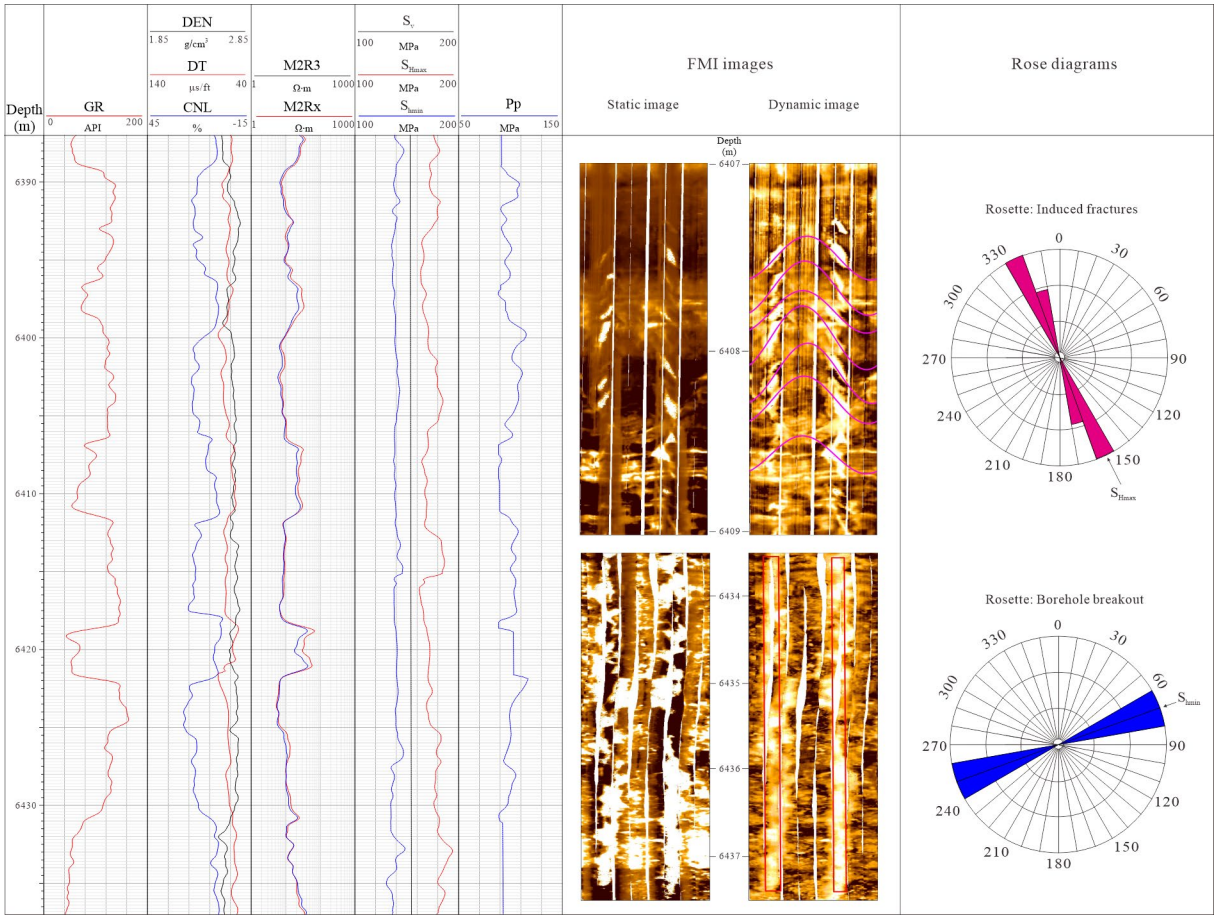

Figure 6: Principal in-situ stresses (S_v, S_{Hmax}, S_{hmin}) and pore pressure (P_p) calculated from a one-dimensional earth stress model. Stress directions were determined by identifying wellbore breakouts and drilling-induced fractures.

5 Discussion

5.1 Sandbody and fracture distribution

5.1.1 Sandstone-mudstone interfaces

Due to the scarcity of core drilling data in Bozi-Dabei zone in Kuqa Depression, image logs are the primary technique for detecting fracture distribution at the interface of sandstone and mudstone. Fractures exhibit a composite pattern characterized by a longer extension when thick sandstone layers coexist with thin mudstone layers (Fig.7a, 7b). Conversely, when thin sandstone layers coexist with thicker mudstone layers, fractures manifest a shorter extension and less favorable connectivity (Fig.7c). The thickness of mudstones is related to the shorter extension of fractures (Fig.7). In conclusion, discrepancies in rock mechanics and relatively thin rock mechanic layers can restrict the formation of fractures.

Sandstones deform less under the same compression than mudstones, leading to localized tensile stress at their boundary due to transverse strain restriction (Biot et al., 1983; He et al., 2024; Gong et al., 2025). The presence of mudstone diminished the density of elastic strain energy in the sandstone at the lithological boundary, thereby limiting the formation of fractures (Feng et al., 2019; Sun et al., 2025).

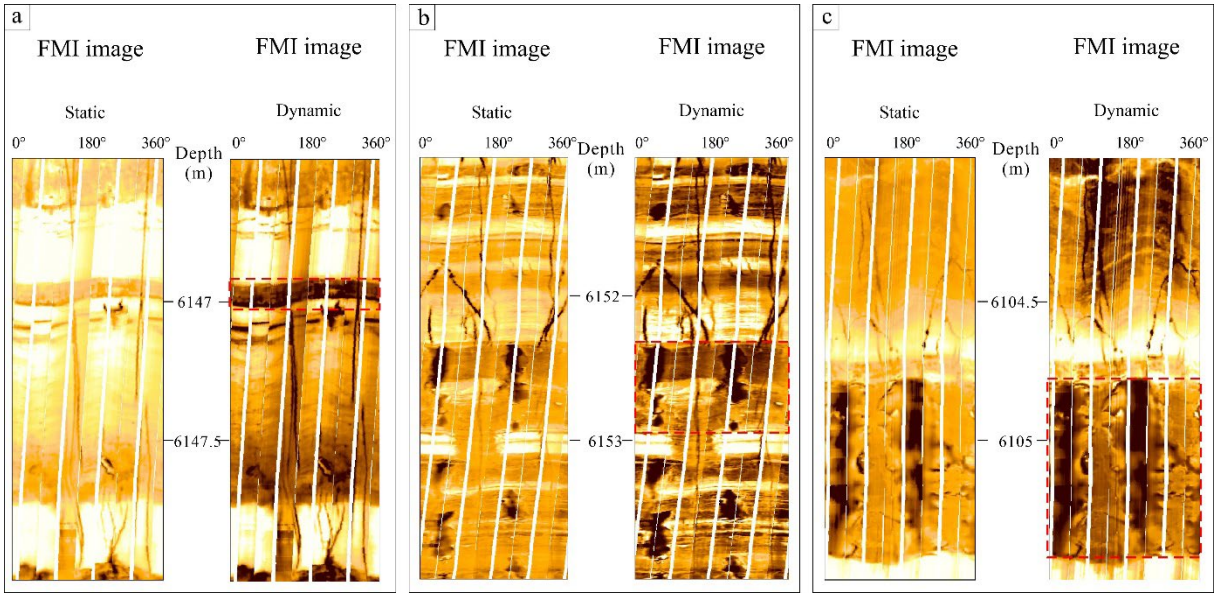

Figure 7: Lithology-controlled fracture characteristics revealed by FMI logs in Bozi-Dabei block, Kuqa Depression

(a) Long, well-connected fracture in thick sandstone interbedded with thin mudstone (6147.5 m)
(b) Restricted fracture propagation in thin sandstone interbedded with thick mudstone (6152 m)
(c) Restricted fracture in thin sandstone interbedded with thick mudstone (6153 m)

5.1.2 Sandbody thickness and fracture

If the sandstones and mudstones suffer the approximate stress field, the elastic strain energy change would be closely related to the thickness (Feng et al., 2019; Smart et al., 2023). Fracture density exhibits an inverse correlation with fractured layer thickness (Fig.8). The thinner the layer, the more concentrated the stress at the fracture tip, and thinner sandbodies are more conducive to forming fractures (Griffith et al, 1921; Nian et al., 2017).

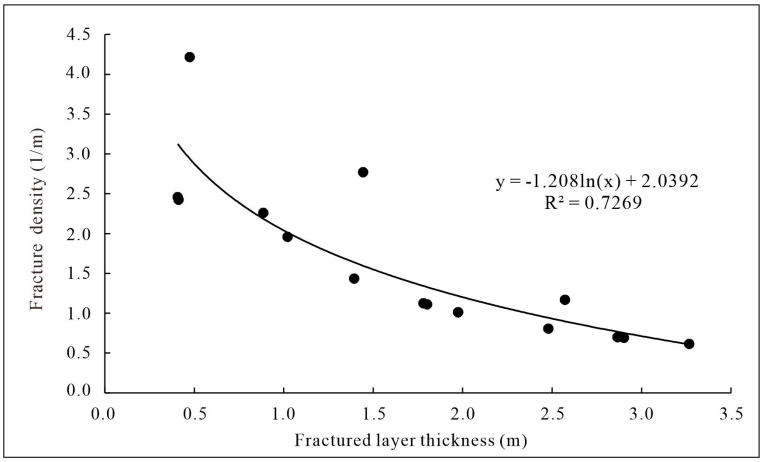

Figure 8: The cross-plot of fractured layer thickness versus fracture density

5.1.3 Fractures in various sandbodies

The interbedding of mudstone and sandstone layers plays a critical role in dictating fracture initiation potential. As illustrated in Figure 8, the mudstone's thickness in contact with the upper formation is a limiting factor for fracture propagation, with only 0.7 m thickness. In contrast, the mudstone thickness interbedded with the lower formation can extend up to 1.5 m, surpassing that of the upper formation. This increased thickness corresponds to a reduced elastic strain energy density, facilitating a higher incidence of forming fractures within the lower formation (Fig.9).

In summary, the lithological composition and sandbody thickness are identified as the primary controlling factors on fracture distribution. The lower sandbody thickness and lower mudstone thickness interfacing with the sandbody, as shown in Figure 8, indicate a higher potential for formation of fractures.

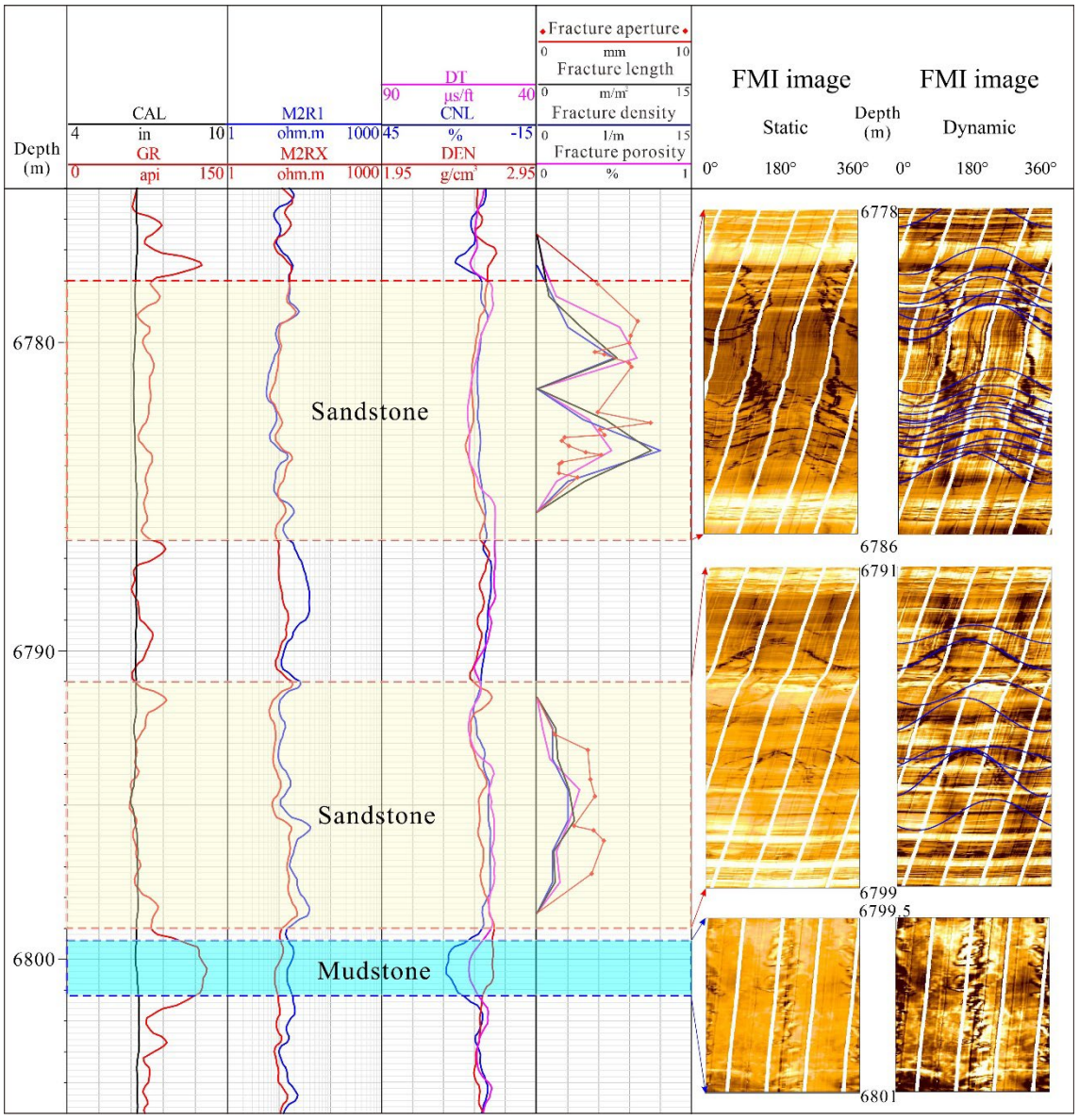

Figure 9: Fracture characteristics in sandbodies of the BZ 104 interval (6778-6801 m). Sandbodies with constant thickness show increased fracture potential where adjacent mudstone is thinner.

325

5.2 Earth stress and fracture distribution

5.2.1 Paleostress and fracture density

Paleostress controls the generation and distribution of natural fractures. The paleostress magnitude is closely related to the formation of fractures (Liu et al., 2018; Zeng et al., 2023; Eichhubl and Aydin, 2023). The direction and intensity of paleostress field directly influence orientation and propagation of fractures within the rock formations (Zhang et al., 2022). By monitoring the material's response to stress, magnitude of maximum paleostress magnitude (σmax) can be obtained using AE tests. Core samples from Bashijiqike formation which are used for AE tests have similar rock composition, and the data indicate a positive correlation between σmax and the fracture density (Fig.10). The high values of fracture density are mainly associated with high magnitude of σmax. In essence, an intensive paleostress is favorable for development of large-scale fractures in sandstones (Zeng et al., 2023).

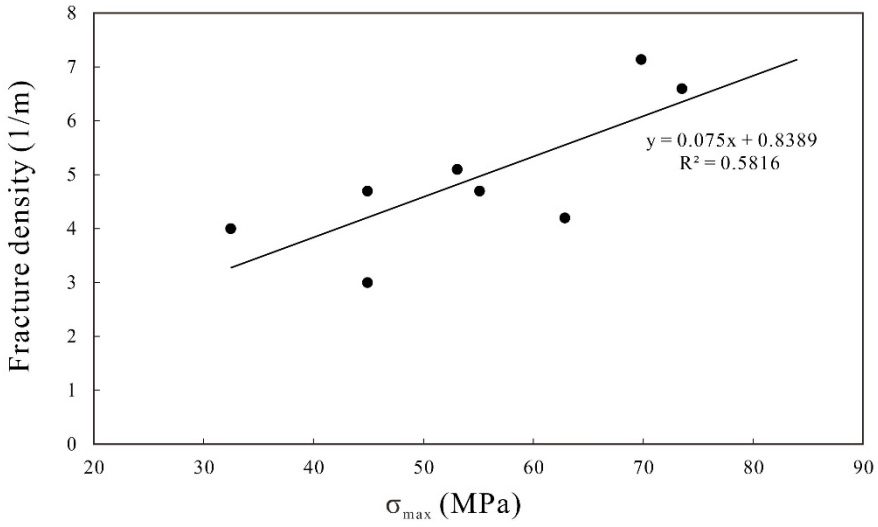

Figure 10: The cross-plot of fracture density versus maximum ancient stress

5.2.2 In situ stress magnitude and fracture distribution

The inverse correlation observed between fracture parameters (aperture and porosity) and the differential stress ratio ($\Delta\sigma/S_{hmin}$) (Fig. 11) indicates that in situ stress conditions may influence fracture characteristics in these sandstones. Lower horizontal stress differences ($\Delta\sigma = S_{Hmax} - S_{hmin}$) appear to correlate with better-preserved fracture apertures. Higher fracture parameters (fracture aperture and porosity) correspond to the lower $\Delta\sigma/S_{hmin}$ ($\Delta\sigma/S_{hmin}=(S_{Hmax}-S_{hmin})/S_{hmin}$) (Fig.11A, Fig.11B). As Δσ/SHmin gets higher, the difference in horizontal principal stresses is more obvious, and the magnitude of fracture parameter gets lower (Fig.11C). These relationships imply that in-situ stress heterogeneity could contribute to fracture distribution patterns, though other factors (mineralization, diagenesis) likely interact with stress controls.

While stress state modulates fracture apertures (e.g., Warpinski, 1987), the preservation of open fractures at high angles to S_{Hmax} suggests additional controls. Mineral bridges (Laubach et al., 2004) and synkinematic cementation (Olson et al., 2009) likely reduced fracture compressibility. Host-rock diagenesis, as evidenced by quartz overgrowths increased matrix modulus (Laubach et al., 2019, Fig. 15), further inhibiting fracture closure. Rapid cementation in high-temperature settings in the Kuqa Depression could sustain fracture porosity despite burial stresses (Wang et al., 2020; Laubach et al., 2023).

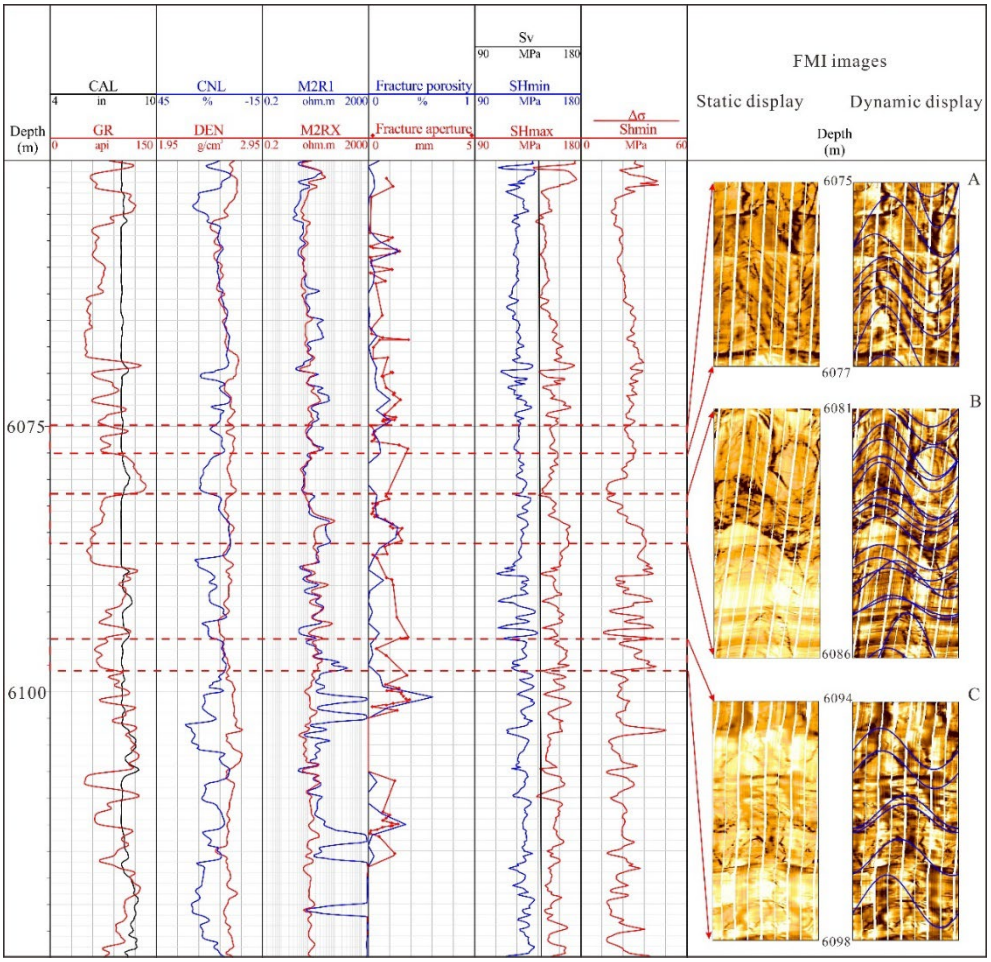

Figure 11: In situ stress magnitude and fracture parameters including fracture porosity and fracture aperture in Well BZ 17. The fracture aperture is higher at the lower $\Delta\sigma/S_{hmin}$ (A, B). The fracture aperture is lower at the higher $\Delta\sigma/S_{hmin}$ (C).

5.3 Fracture distribution within structure positions

The variations of fracture patterns are related to different structural positions in an anticline and fault related anticline. The distribution of fractures is controlled by various structure position (Frehner et al., 2011; Cawood et al., 2023). The fractures are picked out in three wells of the BZ3 wellblock and the fracture parameters were calculated using image logs. The BZ 3 wellblock is located at a large-scale faulted anticline structure (Fig.12). Among them, the well BZ 3 and well BZ 301 are

located near hinge of the anticline. In contrast, Well BZ 302 is located in the limb of the anticline (Fig.12). Due to the use of oil-based mud drilling for BZ3 well, acoustic image log is utilized. The Well BZ 301 also uses oil-based mud for drilling, utilizing the Quatageo logs. However, the Well BZ 302 uses water-based muds for drilling, and the FMI logging tool is used. Affected by oil-based mud, the fractures in well BZ301 are more difficult to identify. Therefore, the fractures identified in BZ 3 and BZ 301 are fewer than the actual ones owing to the influence of oil-based muds using image logs (Fig.12).

The obvious phenomenon can be observed that the fractures detected in the upper strata are significantly more than those detected in the lower strata in each well (Fig.12). The fractures in upper neutral lines of the anticline are more numerous than those in below neutral lines of the anticline (Fig.12). The fractures in below neutral lines of anticline are much less developed, with lower fracture density and lower fracture apertures. Compressive stress tends to reduce the volume of the rock rather than increase the fracture aperture. However, fractures may be more developed due to tensile stress, with potentially higher fracture density and larger apertures in the upper part of an anticline (Jamison et al., 1997; Kim et al., 2022).

The production data and the fracture evaluation demonstrate that the amounts of fractures control the gas production rates and hydrocarbon accumulation conditions of reservoirs. The fracture density is a vital parameter to understand how the structure position controls fracture distribution. The higher fracture density corresponds to higher oil production. In the 5920-5958 m intervals in Well BZ 301, the oil test shows that the daily gas production is 494361 m^3 after blowout through a 7 mm choke whose fracture density is higher (5 /m). However, the daily gas production is 335302 m^3 after blowout through a 6 mm choke in Well BZ 3 whose fracture density is lower (2 /m) in the 5971.5-5985.5 m depth intervals (Fig.12).

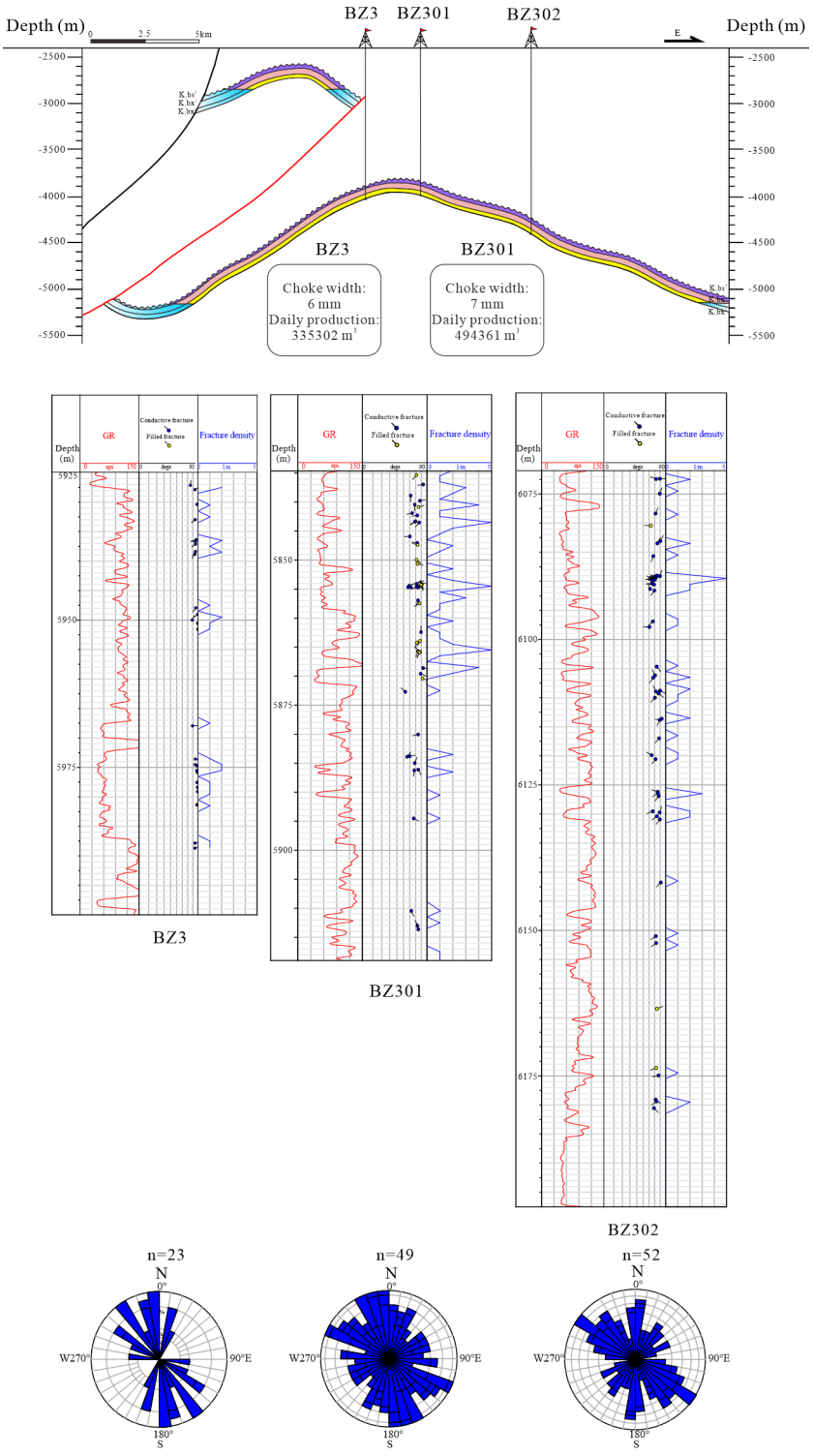

Figure 12: Cross section of BZ 3 as well as fractures interpreted from image logs for BZ 3 wellblock

Meanwhile, the 3 wells located in BZ 12 wellblock are both drilled in oil-based drilling muds. These wells use the same type of drilling muds, and can help evaluate fracture distribution in the anticline structure of the BZ 12 wellblock. The Well BZ 12 zone is located at a faulted-anticline structure. The distribution of fractures is not solely affected by the structural position but is also significantly affected by the proximity to fault, suggesting a complex multifactorial control within the geological setting (Fig.13) (Li et al., 2018). In the hinge of an anticline, due to the compression associated with folding, the concentration of stress is higher, which may lead to rock fracturing and fracture forming. In contrast, in the limbs of an anticline, the stress is more dispersed, hence fewer fractures form (McQuillan, 1973; Ghosh and Mitra, 2009; Cawood et al., 2023).

The amounts of fractures that are detected is the most in the Well BZ 1203, located at the hinge of the anticline, where the calculated fracture density (8/m) is high (Fig.13). In contrast, fewer fractures have been detected within the anticline's limbs, especially at Well BZ 1202. This is consistent with the conclusion that fracture density is strongly controlled by the position at anticlines. However, despite being located in the limb of the anticline, the fracture density at Well BZ 1201 is comparable to that of BZ 1203 in the hinge, as illustrated in Figure 13. The proximity of Well BZ 1201 to the fault is considered a contributing factor to the observed phenomenon. Meanwhile, seismic interpretation reveals that there is a fault near Well BZ 1201 (Fig. 14). This is the reason why, despite being located in the limb of the anticline, the Well BZ 1201 well exhibits a higher fracture density compared to the hinge of the anticline. Fractures are less prevalent in areas that are farther from the fault (Mitchell and Faulkner, 2012; Sun et al., 2021). The data reveal a positive correlation between gas production and fracture density within this geological setting. The high oil production corresponds to higher fracture densities (Fig. 13).

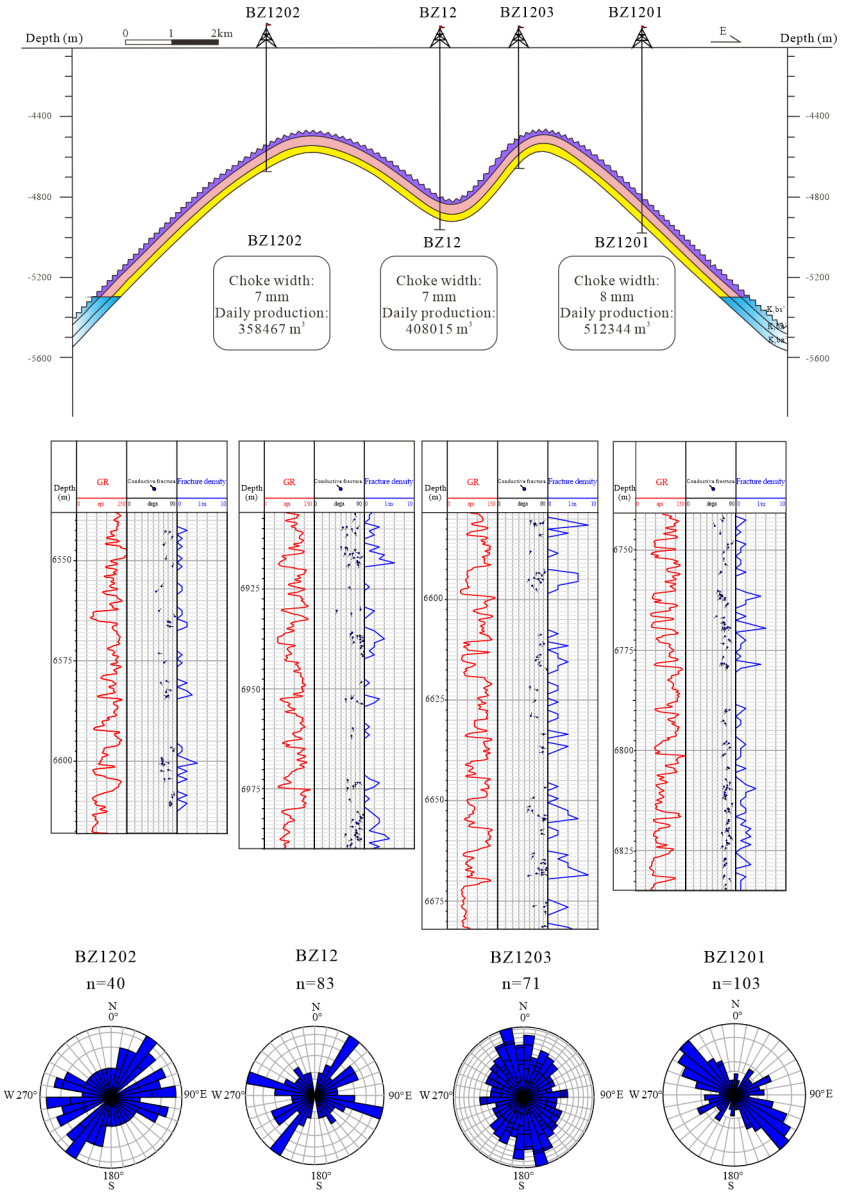

Figure 13: Cross section of BZ 12 as well as fractures interpreted from image logs for BZ 12 wellblock

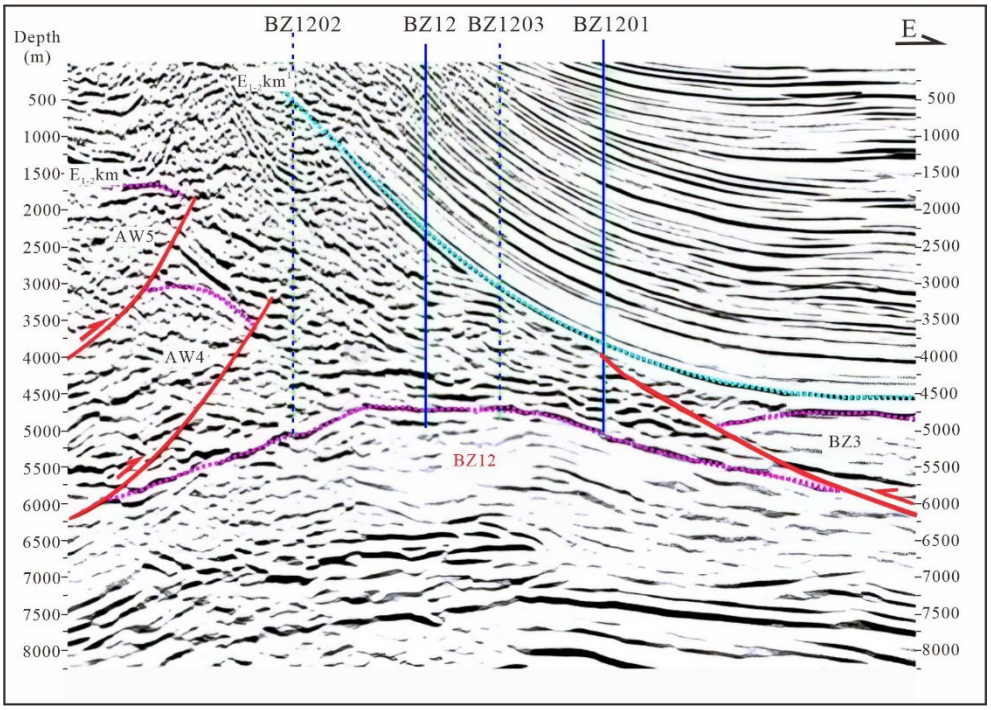

Figure 14: Seismic profile and interpretation showing the main interpreted location of horizons and the faults in the BZ 12 wellblock

5.4 Implication for hydrocarbon exploration

The strain distribution of the anticline can be delineated into three distinct zones including the extensional zone, the transitional zone, and the shortening zone by the presence of two neutral lines (Fig.15) (Frehner, 2011; Li et al., 2018). Then an analysis of the fracture distribution was conducted in the DB 9 wellblock in Kuqa Depression. The fracture distribution correlates with the structural position and will determine the well's production capacity.

The fractures detected in the upper strata above neutral lines, are significantly more than those detected in the lower strata in each well in the DB 9 wellblock. This phenomenon is particularly pronounced in extensional regions, where fracture density is significantly higher than in compressional areas. Notably, the magnitude of fractures is the highest in the well DB 9, which is situated at the hinge of an anticline.

Microscopic examination of thin sections indicates an absence of large pores due to the influence of a strong compressional stress field in well DB 9 (Anders et al., 2014; Li et al., 2018) (Fig.15). However, the presence of tensile fractures in both core samples and thin sections suggests that a regional tensile stress field has likely played a role in forming these open fractures in well DB 9 (Zeng, 2010; Haghi et al., 2019) (Fig.15). The presence of intragranular microfractures in well DB 902 is also related to tectonic compression (Anders et al., 2014) (Fig.15).

Furthermore, the statistics of fracture strikes and dips indicate that both the strikes and dips of fractures vary with structural position. The fracture dips are notably steep in DB 9 wellblock, particularly near the anticline's hinge. In contrast, fractures detected along the limb of the anticline exhibit relatively gentle dips. The strike of fractures in the hinge of the anticline is

oriented in parallel to the hinge line of the anticline owing to the concentration of the stress. However, their characteristics in the wings display relative variability.

The Well DB 9, as depicted in the fracture interpretation from image logs presented in Figure 14, has a higher fracture density. This well has demonstrated exceptional oil and gas productivity. In the 4802-4900 m depth intervals of Well DB 9, the oil test reveals that 511980 m^3 daily natural gas productivity is obtained with 8 mm choke width and drawdown pressure of 60.624 MPa. The High-angle fractures are abundant and the fracture density is higher in this well interval. Grounded in empirical evidence, our study suggests the significant correlation between fracture density and oil production.

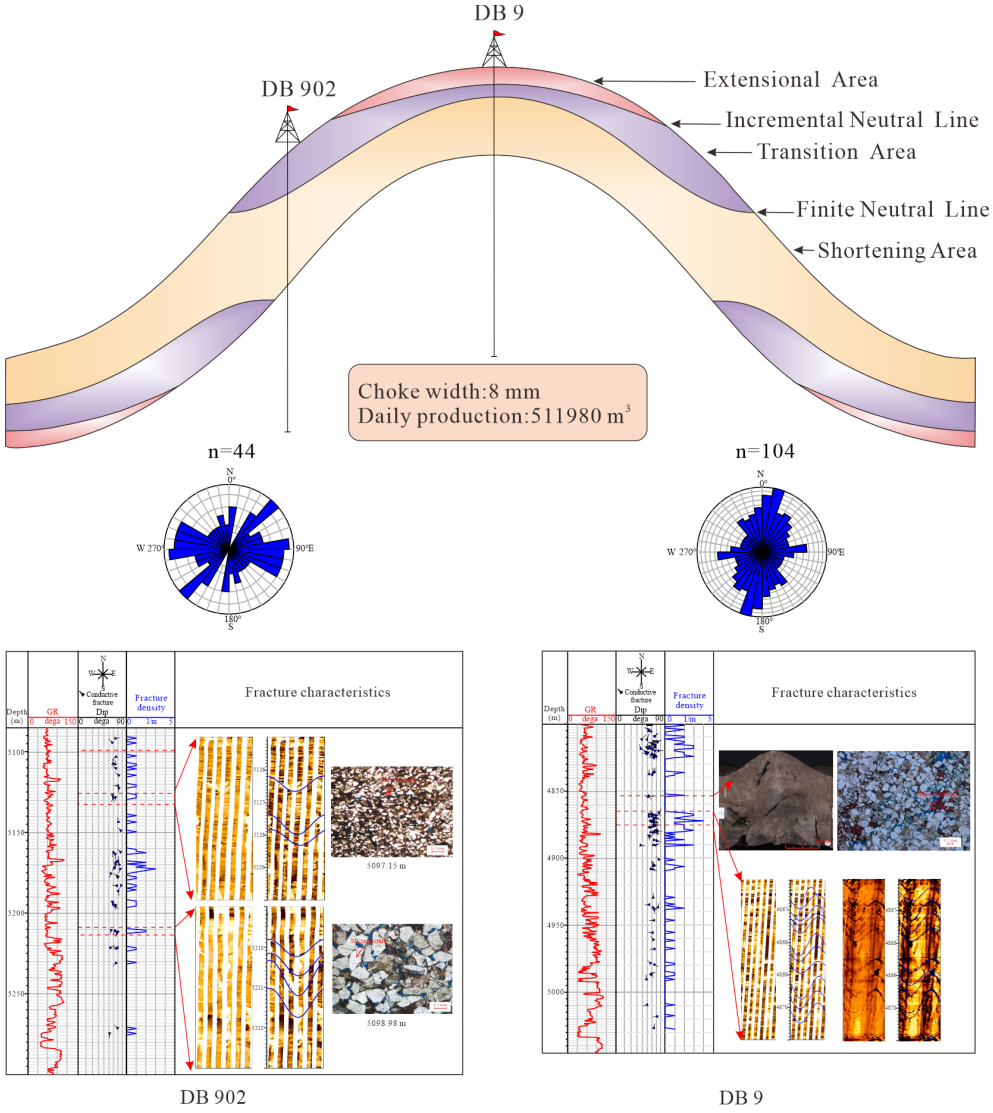

Figure 15: The fracture characteristics in different structure positions in the anticline located at the DB 9 wellblock. Schematic cross-section illustrating three mechanical zones defined by folding: Extensional Area (above the incremental neutral line), Transitional Area (between neutral lines), and Shortening Area (below the finite neutral line) (modified after Frehner, 2011; Li et

al., 2018). Fracture characteristics are observed in two key wells (DB 902 and DB 9) located in the transitional and extensional hinge areas, respectively.

6 Conclusions

This study unravels the geological factors controlling distribution of fractures integrating geological data and geophysical well logs. The fracture types can be categorized into five types including low-angle fractures, horizontal fractures, vertical fractures, high-angle fractures and fracture networks. High-angle fracture is the predominant type in Bozi-Dabei block. Fractures are particularly well-developed in fine-grained sandstones, which is the dominant rock type in the area. Sedimentary factors including sandbody thickness and sandstone-mudstone lithologic interface, are the factors that affect the distribution of fractures. The fracture distribution is inversely related to the sandbody thickness, meaning that thicker sandbody tends to form fewer fractures. Conversely, the presence of thinner sandstones in conjunction with thin mud layers facilitates the formation of fractures. The earth stress is the factor that controls the fracture distribution. The findings indicate a positive correlation between the magnitude of the maximum paleostress and fracture density. An increase in the magnitude of the maximum paleostress corresponds to an increase in fracture density. In situ stress affects the late modification of natural fractures. An increase in the horizontal stress difference, reflecting a greater disparity between the horizontal principal stresses, leads to a decrease in fracture parameter magnitude. Although stress state influences fracture apertures, the preservation of open fractures at high angles to S_{Hmax} indicates additional controlling factors. Consequently, in-situ stress likely interacts with fracture-filling cements to jointly regulate aperture maintenance, rather than serving as the primary control.

The results and approaches of the study have some important implications for the structural position controlling the fracture distribution. Fractures in the hinge of an anticline are more abundant than those in the limbs. The fracture density in the upper formations is higher along the longitudinal axis compared to the fracture density the lower formations. Besides the influence of anticline, fracture density is higher in the formation adjacent to the fault due to the effect of the regional stress field. Additionally, production data demonstrates that the presence of fractures enhances hydrocarbon productivity significantly. The higher fracture density corresponds to higher oil production.

Data availability

The data used to support the findings of this study are available from the corresponding author upon request.

Author contributions

YS, JL and GW contributed to the Conceptualization, Methodology, Software. YS contributed to writing the original draft. WL, XJ and CH contributed to data curation. YJ, ZR and LW contributed to the visualization and investigation. YS, JL and GW contributed to software and validation.

Competing interests

The contact author has declared that neither they nor their co-authors have any competing interests.

Disclaimer

Publisher's note: Copernicus Publications remains neutral with regard to jurisdictional claims in published maps and institutional affiliations.

Acknowledgments

This work is financially supported by National Natural Science Foundation of China (No. 41872133) and Science Foundation of China University of Petroleum, Beijing (No. 2462023QNXZ010). The authors thank PetroChina Tarim Oilfield Company for their data input to this work. We thank Hangzhou Institute of Geology, Research Institute of Petroleum Exploration and PetroChina Tarim Oilfield Company for their work.

Financial support

This work is financially supported by National Natural Science Foundation of China (No. 41872133) and Science Foundation of China University of Petroleum, Beijing (No. 2462023QNXZ010). The authors thank PetroChina Tarim Oilfield Company for their data input to this work. We thank Hangzhou Institute of Geology, Research Institute of Petroleum Exploration and PetroChina Tarim Oilfield Company for their work.

References

Anders, M. H., Laubach, S. E., Scholz, C. H. 2014. Microfractures: A review. Journal of Structural Geology, 69, 377-394.

Barton, C. A., Zoback, M. D., Burns, K. L. 1988. In-situ stress orientation and magnitude at the Fenton geothermal site, New Mexico, determined from wellbore breakouts. Geophysical Research Letters, 15(5), 467-470. https://doi.org/10.1029/GL015i005p00467

Biot, M. A., Medlin, W. L., Masse, L. 1983. Fracture penetration through an interface. Society of Petroleum Engineers Journal, 23(6), 857-869.

Cawood, A. J., Watkins, H., Bond, C. E., Warren, M. J., Cooper, M. A. 2023. Natural fracture patterns at Swift Reservoir anticline, NW Montana: the influence of structural position and lithology from multiple observation scales. Solid earth, 14(9), 1005-1030.

Chen, S. J., Liu, Y., Zhang, J. C., Li, P., Tang, X., Li, Z. M., Dong, Z, Xu, L. F., Zhao, X. X. 2021. Formation conditions and evolution of fractures in multiple tight rocks: Implications for unconventional reservoir exploitation. Journal of Petroleum Science and Engineering, 200, 108354.

Barton, C. A., Zoback, M. D., Moos, D.; Fluid flow along potentially active faults in crystalline rock. 1995. Geology, 23 (8): 683-686.

Douma, L. A. N. R., Regelink, J. A., Bertotti, G., Boersma, Q. D., Barnhoorn, A. 2019. The mechanical contrast between layers controls fracture containment in layered rocks. Journal of Structural Geology, 127, 103856.

Du, H., Ma, B., Wang, C., Han, D., Hu, R. 2025. Pore-fracture fusion modeling method for ultra-deep clastic reservoirs. Marine and Petroleum Geology, 173, 107307.

Eichhubl, P., Aydin, A. 2003. Ductile opening-mode fracture by pore growth and coalescence during combustion alteration of siliceous mudstone. Journal of Structural Geology, 25(1), 121-134.

Feng, J., Liu, S., Du, H., Liu, H. 2023. Quantitative prediction of ultra-deep tight sandstone fractures based on the theory of minimum energy dissipation. Geoenergy Science and Engineering, 226, 211749.

Feng, J., Shi, S., Zhou, Z., Li, X., Luo, P. 2019. Characterizing the influence of interlayers on the development and distribution of fractures in deep tight sandstones using finite element method. Journal of Structural Geology, 123, 81-95.

Frehner, M. 2011. The neutral lines in buckle folds. Journal of Structural Geology, 33(10), 1501-1508.

Friedman, M. 1969. Structural Analysis of Fractures in Cores from Saticoy Field, Ventura County, California1. AAPG Bulletin, 53(2), 367-389.

Gale, J. F., Laubach, S. E., Olson, J. E., Eichhubl, P., Fall, A. 2014. Natural fractures in shale: A review and new observations. AAPG Bulletin, 98(11), 2165-2216.

Ghosh, K., Mitra, S. 2009. Structural controls of fracture orientations, intensity, and connectivity, Teton anticline, Sawtooth Range, Montana. AAPG Bulletin, 93(8), 995-1014.

Gong, L., Liu, G., Wang, R., Dong, S., Wu, Z. 2025. Editorial: Distribution and Development of Faults and Fractures in Shales. Minerals, 15(11), 1154.

Griffith, A. A. 1921. VI. The phenomena of rupture and flow in solids. Philosophical transactions of the royal society of london. Series A, containing papers of a mathematical or physical character, 221(582-593), 163-198.

Guo, P., Ren, D., Xue, Y. 2019. Simulation of multi-period tectonic stress fields and distribution prediction of tectonic fractures in tight gas reservoirs: A case study of the Tianhuan Depression in western Ordos Basin, China. Marine and Petroleum Geology, 109, 530-546.

Guo, X., Liu, K., Jia, C., Song, Y., Zhao, M., Zhuo, Q., Lu, X. 2016. Constraining tectonic compression processes by reservoir pressure evolution: Overpressure generation and evolution in the Kelasu Thrust Belt of Kuqa Foreland Basin, NW China. Marine and Petroleum Geology, 72, 30-44.

Haghi, A. H., Chalaturnyk, R., Talman, S. 2019. Stress-dependent pore deformation effects on multiphase flow properties of porous media. Scientific Reports, 9(1), 15004.

Hanks, C. L., Lorenz, J., Teufel, L., Krumhardt, A. P. 1997. Lithologic and structural controls on natural fracture distribution and behavior within the Lisburne Group, northeastern Brooks Range and North Slope subsurface, Alaska. AAPG Bulletin, 81(10), 1700-1720.

He, Z., Wu, G., Zhu, J. 2024. Mechanical properties of rock under uniaxial compression tests of different control modes and loading rates. Scientific Reports, 14(1), 2164.

Jamison, W. R. 1997. Quantitative Evaluation of Fractures on Monkshood Anticline, a Detachment Fold in the Foothills of Western Canada1. AAPG Bulletin, 81(7), 1110-1132.

Jia, C. Z., Li, Q. M. 2008. Petroleum geology of Kela-2, the most productive gas field in China. Marine and Petroleum Geology, 25(4-5), 335-343.

Ju, W., Hou, G., Zhang, B. 2014. Insights into the damage zones in fault-bend folds from geomechanical models and field data. Tectonophysics, 610, 182-194.

Ju, W., Wang, K. 2018. A preliminary study of the present-day in-situ stress state in the ahe tight gas reservoir, dibei gasfield, kuqa depression. Marine and Petroleum Geology, 96, 154-165.

Kaiser J., 1953. Erkenntnisse und Folgerungen aus der Messung von Geräuschen bei Zugbeanspruchung von metallischen Werkstoffen, Arch. Eisenhütten., 24, 1-2.

Kim, I., Park, S. I., Kwon, S., Lee, H. J. 2022. Evolution of fracture networks and connectivity during fault–bend folding: Insights from the Sinon Anticline in the southwestern Hongseong–Imjingang Belt, Korea. Journal of Structural Geology, 155, 104506.

Koerperich, E. A. 1978. Investigation of Acoustic Boundary Waves And Interference Patterns as Techniques for Detecting Fractures. Journal of Petroleum Technology, 30(8), 1199-1207.

Lai J., Su Y., Xiao L., Zhao F., Bai T., Li Y., Li H., Huang Y., Wang G., Qin Z. 2024. Application of geophysical well logs in solving geologic issues: Past, present and future prospect. Geoscience Frontiers, 15, 101779.

Lai J., Wang G., Chai Y., Xin Y., Wu Q., Zhang X., Sun Y. 2017. Deep burial diagenesis and reservoir quality evolution of high-temperature, high-pressure sandstones: Examples from Lower Cretaceous Bashijiqike Formation in Keshen area, Kuqa depression, Tarim basin of China. AAPG Bulletin, 101(6): 829–862.

Lai J., Wang G., Fan Q., Zhao F., Zhao X., Li Y., Zhao Y., Pang X. 2023. Towards the scientific interpretation of geophysical well logs: typical misunderstandings and countermeasures. Surveys in Geophysics, 44: 463-494

Lai, J., Chen, K., Xin, Y., Wu, X., Chen, X., Yang, K., Song, Q., Wang, G., Ding, X. 2021. Fracture characterization and detection in the deep Cambrian dolostones in the Tarim Basin, China: Insights from borehole image and sonic logs. Journal of Petroleum Science and Engineering, 196, 107659.

Lai, J., Li, D., Wang, G., Xiao, C., Hao, X., Luo, Q., Lai, L., Qin, Z. 2019. Earth stress and reservoir quality evaluation in high and steep structure: The Lower Cretaceous in the Kuqa Depression, Tarim Basin, China. Marine and Petroleum Geology, 101, 43-54.

Lai, J., Wang, G., Wang, S., Cao, J., Li, M., Pang, X., Han, C., Fan, X., Yang, L., He, Z., Qin, Z. 2018. A review on the applications of image logs in structural analysis and sedimentary characterization. Marine and Petroleum Geology, 95, 139-166.

Lander, R. H., Laubach, S. E. 2015. Insights into rates of fracture growth and sealing from a model for quartz cementation in fractured sandstones. GSA Bulletin, 127(3-4), 516-538.

Laubach, S. E. 2003. Practical approaches to identifying sealed and open fractures. AAPG Bulletin, 87(4), 561-579.

Laubach, S. E., Lander, R. H., Criscenti, L. J., Anovitz, L. M., Urai, J. L., Pollyea, R. M., et al. 2019. The role of chemistry in fracture pattern development and opportunities to advance interpretations of geological materials. Reviews of Geophysics. 57, 1065-1111.

Laubach, S. E., Olson, J. E., Gross, M. R. 2009. Mechanical and fracture stratigraphy. AAPG Bulletin, 93(11), 1413-1426.

Laubach, S.E., Olson, J.E., and Gale, J.F.W., 2004, Are open fractures necessarily aligned with maximum horizontal stress? Earth & Planetary Science Letters, 222/1, 191-195.

Laubach, S.E., Zeng, L., Hooker, J.N., Wang, Q., Zhang, R.H., Wang., J., Ren, B., 2023. Deep and ultra-deep basin brittle deformation with focus on China. Journal of Structural Geology 175, 104938

Lavrov, A. 2003. The Kaiser effect in rocks: Principles and stress estimation techniques. International Journal of Rock Mechanics and Mining Sciences, 40(2), 151-171.

Li, P., Lee J., Taher A., Coates R., Marlow R. 2019. “New 4 3/4-In. High-Resolution Ultrasonic Borehole Imaging for Unconventional Reservoir Evaluation.” In Unconventional Resources Technology Conference, Denver, Colorado, 22-24 July 2019, SEG Global Meeting Abstracts, Unconventional Resources Technology Conference (URTeC); Society of Exploration Geophysicists, 43–61.

Li, Y. J., Wen, L., Zhang, H. A., Huang, T. Z., Li, H. L., Shi, Y. Y., Meng, Q. L., Peng, G. X., Huang, S. Y., Zhang, Q. 2016. The Kuqa late Cenozoic fold–thrust belt on the southern flank of the Tian Shan Mountains. International Journal of Earth Sciences, 105(5), 1417-1430.

Li, Y., He, J., Deng, H., Li, R., Li, Q., Fu, M., Yu, Y. 2024. Effect of lithofacies assemblages on multi-scale fractures in the transitional shale and its implications for shale gas exploration. Geoenergy Science and Engineering, 233, 212562.

Li, Y., Hou, G., Hari, K. R., Neng, Y., Lei, G., Tang, Y., Zhou, L., Sun, S., Zheng, C. 2018. The model of fracture development in the faulted folds: The role of folding and faulting. Marine and Petroleum Geology, 89, 243-251.

Liu, J., Ding, W., Gu, Y., Xiao, Z., Dai, J., Dai, P., Chen, X., Zhao, G. 2018. Methodology for predicting reservoir breakdown pressure and fracture opening pressure in low-permeability reservoirs based on an in situ stress simulation. Engineering Geology, 246, 222-232.

Lucca, A., Ogata, K., Balsamo, F., Borsani, A., Clemenzi, L., Hatushika, R., Tinterri, R., Storti, F. 2024. Sedimentary facies control on fracture and mechanical stratigraphy in siliciclastics: Marnoso-arenacea formation, Northern Apennines, Italy. Marine and Petroleum Geology, 167, 106927.

Lyu, W., Zeng, L., Liu, Z., Liu, G., Zu, K. 2016. Fracture responses of conventional logs in tight-oil sandstones: A case study of the Upper Triassic Yanchang Formation in southwest Ordos Basin, China. AAPG Bulletin, 100(9), 1399-1417.

McQuillan, H. 1973. Small-Scale Fracture Density in Asmari Formation of Southwest Iran and Its Relation to Bed Thickness and Structural Setting1. AAPG Bulletin 57(12): 2367-85.

Medici, G., Munn, J.D. and Parker, B.L., 2024. Delineating aquitard characteristics within a Silurian dolostone aquifer using high-density hydraulic head and fracture datasets. Hydrogeology Journal, 32(6), 1663-1691.

Mercuri, M., Carminati, E., Tartarello, M. C., Brandano, M., Mazzanti, P., Brunetti, A., McCaffrey, K. J. W., & Collettini, C. 2020. Lithological and structural control on fracture frequency distribution within a carbonate-hosted relay ramp. Journal of Structural Geology, 137, 104085.

Mitchell, T. M., Faulkner, D. R. 2012. Towards quantifying the matrix permeability of fault damage zones in low porosity rocks. Earth and Planetary Science Letters, 339-340, 24-31.

Nelson, R. A. 1985. Geologic analysis of naturally fractured reservoirs (Vol. 1). Gulf Professional Publishing.

Nian, T., Wang, G., Song, H. 2017. Open tensile fractures at depth in anticlines: A case study in the Tarim basin, NW China. Terra Nova, 29(3), 183-190.

Ogata, K., Storti, F., Balsamo, F., Tinterri, R., Bedogni, E., Fetter, M., Gomes, L., Hatushika, R. 2017. Sedimentary facies control on mechanical and fracture stratigraphy in turbidites. GSA Bulletin, 129(1-2), 76-92.

Olson, J. E., Laubach, S. E., and Lander, R. L., 2007, Combining diagenesis and mechanics to quantify fracture aperture distributions and fracture pattern permeability: In Lonergan, L., Jolley, R.J., Sanderson, D.J., Rawnsley, K., eds., Fractured Reservoirs, Geological Society of London Special Publication 270, 97-112.

Olson, J. E., Laubach, S. E., Lander, R. H. 2009. Natural fracture characterization in tight gas sandstones: Integrating mechanics and diagenesis. AAPG Bulletin, 93(11), 1535-1549.

Pang, X., Wang, G., Kuang, L., Lai, J., Mountney, N. P. 2024. Investigation of Fluid Types in Shale Oil Reservoirs. Surveys in Geophysics.

Qiu, N., Chang, J., Zuo, Y., Wang, J., Li, H. 2012. Thermal evolution and maturation of lower Paleozoic source rocks in the Tarim Basin, northwest China. AAPG Bulletin, 96(5), 789-821.

Rajabi M., Sherkati S., Bohloli B., Tingay M., 2010. Subsurface fracture analysis and determination of in-situ stress direction using FMI logs: An example from the Santonian carbonates (Ilam Formation) in the Abadan Plain, Iran. Tectonophysics 492, 192-200.

Romano, V., Proietti, G., Pawar, R.J., Bigi, S. 2025. Evaluation of fracture network efficiency to CO2 storage with a DFN approach. International Journal of Greenhouse Gas Control, 141, 104317.

Smart, K. J., Ferrill, D. A., Morris, A. P. 2023. Geomechanical insights on the importance of mechanical stratigraphy to hydraulic fracture containment. AAPG Bulletin, 107(10), 1811-1835.

Su, X., Zhu, R., Zhang, J., Liu, C., Gong, L., Jiang, X., Fu, X., Ostadhassan, M. 2025. Multi-scale characterization and control factors of bedding-parallel fractures in continental shale reservoirs: Insights from the Qingshankou formation, Songliao basin, China. Marine and Petroleum Geology, 182, 107580.

Sun, X., Gomez-Rivas, E., Alcalde, J., Martín-Martín, J. D., Ma, C., Muñoz-López, D., Cruset, D., Cantarero, I., Griera, A., Travé, A. 2021. Fracture distribution in a folded fluvial succession: The Puig-reig anticline (south-eastern Pyrenees). Marine and Petroleum Geology, 132, 105169.

Tingay, M., Reinecker, J., Müller, B., 2008. Borehole breakout and drilling-induced fracture analysis from image logs. World Stress Map Project 1-8. Guidelines: Image logs.

Tingay, M.R.P., Hillis, R.R., Morley, C.K., King, R.C., Swarbrick, R.E., Damit, A.R., 2009. Present-day stress and neotectonics of Brunei: implications for petroleum exploration and production. AAPG Bull. 93, 75-100.

Warpinski, N.R., and L.W. Teufel. 1987. Influence of Geologic Discontinuities on Hydraulic Fracture Propagation (includes associated papers 17011 and 17074). Journal of Petroleum Technology, 39: 209-220

Xu, X. T., Zeng, L. B., Dong, S.Q., Li, H. M., Liu, J. Z., Ji, C. Q. 2025. The characteristics and controlling factors of high-quality reservoirs of ultra-deep tight sandstone: A case study of the Dabei gas field, Tarim Basin, China. Petroleum Science. Available online 24 March 2025

Yang, K., Xu, L., Qi, J., He, P., Du, J., Sun, T. 2023. Structural deformation of the Northern Monocline belt in the Kuqa depression and implications for the Cenozoic uplift history of the South Tianshan Mountains. Tectonophysics, 857, 229840.

Yang, Y., Li, X., Yang, X., Li, X. 2022. Influence of reservoirs/interlayers thickness on hydraulic fracture propagation laws in low-permeability layered rocks. Journal of Petroleum Science and Engineering, 219, 111081.

Yu, G., Liu, K., Xi, K., Yang, X., Yuan, J., Xu, Z., Zhou, L., Hou, S. 2023. Variations and causes of in-situ stress orientations in the Dibei-Tuziluoke gas field in the Kuqa foreland basin, western China. Marine and Petroleum Geology, 158, 106528.

Yu, S., Chen, W., Evans, N. J., McInnes, B. I. A., Yin, J., Sun, J., Li, J., 2014. Cenozoic uplift, exhumation, and deformation in the north Kuqa Depression, China as constrained by (U-Th)/He thermochronometry. Tectonophysics, 630, 166-182.

Zahmatkesh, I., Soleimani, B., Kadkhodaie, A., Golalzadeh, A., Abdollahi, A.-M. 2017. Estimation of DSI log parameters from conventional well log data using a hybrid particle swarm optimization–adaptive neuro-fuzzy inference system. Journal of Petroleum Science and Engineering, 157, 842-859.

Zeng, L. 2010. Microfracturing in the Upper Triassic Sichuan Basin tight-gas sandstones: Tectonic, overpressure, and diagenetic origins. AAPG Bulletin, 94(12), 1811-1825.

Zeng, L., Gong, L., Zhang, Y., Dong, S., Lyu, W. 2023. A review of the genesis, evolution, and prediction of natural fractures in deep tight sandstones of China. AAPG Bulletin, 107(10), 1687-1721.

Zeng, L., Su, H., Tang, X., Peng, Y., Gong, L. 2013. Fractured tight sandstone oil and gas reservoirs: A new play type in the Dongpu depression, Bohai Bay Basin, China. AAPG Bulletin, 97(3), 363-377.

Zhang, D., Tang, J., Chen, K., Wang, K., Zhang, P., He, G., Tuo, X. 2022. Simulation of tectonic stress field and prediction of tectonic fracture distribution in Longmaxi Formation in Lintanchang area of eastern Sichuan Basin. Frontiers in Earth Science, 10, 1024748.

Zhang, G., Liu, J., Xu, K., Jiang, S., Zhang, B., Shi, N. 2024. Characteristics and effectiveness of deep and ultradeep tight sandstone fractures: Insights from geological and geophysical data analysis. Geophysics, 89(5), 1-55.

Zhang, S., Ma, X. 2021. How does in situ stress rotate within a fault zone? Insights from explicit modeling of the frictional, fractured rock mass. Journal of Geophysical Research: Solid Earth, 126(11), e2021JB022348.

Zhao, F., Shi, Z., Yu, S., Zheng, H. 2023. A review of fracture mechanic behaviors of rocks containing various defects. Underground Space, 12, 102-115.

Zhao, Z., He, Y., Huang, X. 2021. Study on Fracture Characteristics and Controlling Factors of Tight Sandstone Reservoir: A Case Study on the Huagang Formation in the Xihu Depression, East China Sea Shelf Basin, China. Lithosphere, 2021(Special 1), 3310886.

Zoback MD. Reservoir Geomechanics. Cambridge University Press; 2007.

Zoback, M. D., Barton, C. A., Brudy, M., Castillo, D. A., Finkbeiner, T., Grollimund, B. R., Moos, D. B., Peska, P., Ward, C. D., Wiprut, D. J. 2003. Determination of stress orientation and magnitude in deep wells. International Journal of Rock Mechanics and Mining Sciences, 40(7), 1049-1076.